

Cross-Scale Modeling of Storm-Time Radiation Belt Variability

A. T. Michael¹, K. A. Sorathia¹, A.Y. Ukhorskiy¹, J. Albert², X. Shen³, W. Li³, V.G. Merkin¹

¹The Johns Hopkins University Applied Physics Laboratory, Laurel, MD, USA

²Air Force Research Laboratory, Albuquerque, NM, USA

³Boston University, Boston, MA, USA

Key Points:

- We developed a novel global test particle model of storm-time radiation belt dynamics with local wave-particle interactions.
- Evolution of the magnetic field and density yields local variations of the magnitude and resonant energy of the wave-particle interactions.
- The newly developed capability enables separation of electron acceleration and loss processes driven by both transport and local wave-particle interactions.

Abstract

During geomagnetic storms relativistic outer radiation belt electron flux exhibits large variations on rapid time scales of minutes to days. Many competing acceleration and loss processes contribute to the dynamic variability of the radiation belts; however, distinguishing the relative contribution of each mechanism remains a major challenge as they often occur simultaneously and over a wide range of spatiotemporal scales. In this study, we develop a new comprehensive model for the storm-time radiation belt dynamics by incorporating electron wave-particle interactions with parallel propagating whistler mode waves into our global test-particle model of the outer belt. Electron trajectories are evolved through the electromagnetic fields generated from the Multiscale Atmosphere Geospace Environment (MAGE) global geospace model. Pitch angle scattering and energization of the test particles are derived from analytical expressions for quasi-linear diffusion coefficients that depend directly on the magnetic field and density from the magnetosphere simulation. Using a case study of the 17 March 2013 geomagnetic storm, we demonstrate that resonance with lower band chorus waves can produce rapid relativistic flux enhancements during the main phase of the storm. While electron loss from the outer radiation belt is dominated by loss through the magnetopause, wave-particle interactions drive significant atmospheric precipitation. We also show that the storm-time magnetic field and cold plasma density evolution produces strong, local variations of the magnitude and energy of the wave-particle interactions and is critical to fully capturing the dynamic variability of the radiation belts caused by wave-particle interactions.

Plain Language Summary

1 Introduction

Relativistic electron intensities in Earth's outer radiation belt are highly dynamic. During geomagnetic storms, electron intensities in the outer belt can vary over an order of magnitude on rapid time scales of minutes to days and across a wide range of L -shells (See reviews by W. Li & Hudson, 2019; Ripoll et al., 2020). The system response of the radiation belts is highly non-linear. Geomagnetic storms can cause a net-enhancement, depletion, or no relative change in the relativistic electron fluxes in relation to pre-storm levels (Reeves et al., 2003).

Many competing acceleration and loss processes contribute to the dynamic variability of the radiation belts. Acceleration, transport, and loss occur primarily through two different processes: radial transport and/or via local resonant wave-particle interactions. Radial transport energizes electrons via conservation of the first and second adiabatic invariant (Schulz, 1974) when it acts at time scales longer than the typical bounce motion of trapped electrons across large spatial scales. Transport processes include convection from the plasma sheet, including mesoscale ($\sim 1 R_E$) injections associated with fast flows (Gabrielse et al., 2017; Turner et al., 2017), particle injections induced by interplanetary shocks (Foster et al., 2015), and resonant interactions with ultra-low frequency (ULF) waves. Local wave-particle interactions violate the 1st and 2nd adiabatic invariant through gyroresonance, resulting in pitch angle scattering of the electrons and energy transfer between the electrons and the waves. Local wave-particle interactions act on time scales comparable to the electron gyroperiod and cause localized enhancements in phase space density (PSD) at L -shells where waves are present. Many different wave modes can resonate with radiation belt electrons (See reviews by Shprits, Subbotin, et al. (2008); Thorne (2010); W. Li and Hudson (2019); Ripoll et al. (2020)). Whistler mode chorus waves are generated outside of the plasmapause (Malaspina et al., 2016) and have been shown to produce significant flux enhancements in the outer radiation belts (Horne et al., 2003; Summers et al., 2007b). Both radial transport and wave-particle interactions are substantially enhanced during geomagnetic storms and can lead to permanent electron loss from the system. Electron loss occurs either via particle escape through

the magnetopause boundary or by particle scattering into the loss cone and subsequent precipitation into the atmosphere (e.g., Millan & Thorne, 2007; Shprits, Elkington, et al., 2008; Shprits, Subbotin, et al., 2008, and references therein).

Mesoscale particle injections and wave-particle interactions often occur simultaneously, and interact in a complex manner. For instance, Jaynes et al. (2015) suggested that substorm injections increase two key populations in the outer radiation belt: the source population (1-10s of keV), which provides free energy for the growth of chorus waves, and the seed population of electrons (10s-100s keV), which are then rapidly accelerated by the chorus waves to relativistic energies. Statistical surveys of plasma wave and particle data have found that significant relativistic electron flux enhancements occur outside the plasmapause, in association with prolonged substorm activity, enhanced fluxes of seed electrons, and increased levels of chorus wave activity (Meredith et al., 2003). Furthermore, ultra-relativistic electron flux enhancements are more likely to occur during intense geomagnetic storms when substorm activity is present (Zhao et al., 2019).

Distinguishing relative contributions of the different acceleration and loss processes that govern radiation belt dynamics remains a major challenge. The large spatial, temporal, and energy ranges over which radial transport and wave-particle interactions act are difficult for both observations and numerical models to resolve. Several approaches have been used to simulate radiation belt dynamics. One common method is 3D diffusion models based upon the quasi-linear approximation. Diffusion models of the radiation belts solve the Fokker-Planck equation by reducing electron dynamics to three-dimensional diffusion in pitch angle, energy, and L -shell through gyro-, bounce, and drift averaging of the solution. Diffusion models can account for local pitch-angle scattering, particle energization, and loss due to the combined effect of multiple wave modes interacting with electrons (See review by Ripoll et al., 2020, and references therein). The drift-bounce averaged transport associated with Fokker-Planck diffusion models, however, is only applicable on timescales much longer than the drift period (Ukhorskiy & Sitnov, 2013). Diffusion models, therefore, do not encompass the full range of physical processes that govern the storm-time evolution of the outer belt. In particular, diffusion models do not capture the effects of rapid, large-scale reconfiguration of the magnetic field in storm main phase that causes rapid non-adiabatic expansion of electron drift orbits and subsequent magnetopause loss of particles from a broad range of L -shells (Ukhorskiy et al., 2006; Staples et al., 2022). In addition, the inward radial transport is not always slow. During storms, earthward convection can occur in the form of mesoscale bursty bulk flows (BBFs) (Baumjohann et al., 1990; Angelopoulos et al., 1994) that swiftly transport source and seed electrons through localized azimuthal electric fields and magnetic gradient trapping (Gabrielse et al., 2017; Ukhorskiy et al., 2018; Sorathia et al., 2018; Turner et al., 2021; Kim et al., 2023). Furthermore, boundary layer dynamics on the magnetopause cause additional loss to occur through Kelvin-Helmholtz waves (Sorathia et al., 2017), complicating loss estimated through the last closed drift shell.

A more detailed description of electron transport in the outer radiation belt is provided by test-particle simulations. Test-particle simulations evolve relativistic electrons through accurate, time-varying electromagnetic fields provided by global magnetosphere models and can, therefore, describe the full range of three-dimensional effects, including rapid, non-diffusive radial transport. These effects include key loss and acceleration processes due to: magnetosonic waves driven by coronal mass ejections (CMEs) (Hudson et al., 2015), drift orbit bifurcations (Ukhorskiy et al., 2011), expansion of electron drift orbits in response to large-scale magnetic field perturbations due to the storm-time ring current (Ukhorskiy et al., 2006), injections from magnetotail convection and fast, mesoscale flows (Ukhorskiy et al., 2018; Sorathia et al., 2018; Sorathia et al., 2021), ULF waves (Claudepierre et al., 2016) and their associated radial transport (Kress et al., 2012), and losses associated with magnetopause boundary dynamics, such as additional loss mediated by Kelvin-Helmholtz waves (Sorathia et al., 2017). Using global magnetosphere and test particle

simulations, Sorathia et al. (2018) captured the initial dropout of the radiation belts and subsequent rebuilding through injections in the tail during the 17 March 2013 geomagnetic storm. The test particle simulations obtained good quantitative agreement for radiation belt intensities below 1 MeV throughout all phases of the storm. There were, however, large discrepancies between the modeled intensity and observation at the multi-MeV energies, where the model intensity had a weaker overall enhancement. One possible reason for this discrepancy is that test-particle simulations used in those simulations did not account for local pitch-angle scattering and energization by kinetic plasma waves.

Chan et al. (2023) incorporated the effects of cyclotron-resonant wave-particle interactions into their global magnetosphere and test-particle simulation by using a stochastic differential equation (SDE) to solve the Fokker-Planck equation (Tao et al., 2008; Zheng et al., 2014, 2021). Pitch-angle scattering and energy diffusion were calculated using pre-computed, event-specific bounce-averaged diffusion coefficients from Ma et al. (2018). Chan et al. (2023) showed local acceleration can result in rapid changes in PSD and, combined with radial diffusion, and can produce electron PSD enhancements in the outer radiation belts. However, the bounce-averaged diffusion coefficients used in Chan et al. (2023), were computed using a dipolar magnetic field and a static density distribution. The diffusion coefficients, therefore, did not exhibit a realistic variability due to either the storm-time magnetic field or the cold plasma density, which can significantly affect both the estimated wave power (Longley et al., 2022) and the characteristics of the wave-particle interactions themselves (e.g., Kennel & Petschek, 1966).

The goal of this study is to incorporate wave-particle interactions into our global test particle simulation in a physically consistent way to directly connect local acceleration and scattering effects to the background plasma and wave fields. This is done within a modular framework to be able to isolate and analyze the relative importance of each loss and acceleration mechanism governing radiation belt dynamics. In this paper, we analyze the main phase of the 17 March 2013 geomagnetic storm and investigate the impact that field-aligned chorus waves have on radiation belt variability. The paper is structured as follows. A description of the numerical models used in this study is presented in Section 2. Section 2.3 describes how the empirical wave model of lower band chorus waves is assimilated into the simulation. Section 2.4 and Appendix B detail the algorithm used to calculate resonant interactions in the test particle model, and Section 3 gives an overview of the 17 March 2013 storm and the application of the model to simulate the event. Section 4 presents our results. Section 4.1 provides an analysis of how the storm-time magnetic field and density create an magnetic local time (MLT) and energy dependence in the quasi-linear diffusion coefficients. Section 4.2 describes the resulting enhancement of multi-MeV electron fluxes at the beginning of the recovery phase and Section 4.3 presents quantitative comparisons of the varying storm-time loss processes. Finally, Section 5 discusses the implications of our results on radiation belt dynamics and provides a summary.

2 Methodology

To fully capture storm-time evolution of the radiation belts, it is necessary to account for the full range of acceleration and transport processes that can be both diffusive and non-diffusive. For this purpose, we combine the Fokker-Planck formalism for local resonant wave-particle interactions and our global test-particle radiation belt model that accurately capture storm-time global-to-mesoscale dynamics (Sorathia et al., 2018). The implemented numerical scheme solves the diffusion equation for pitch angle scattering and acceleration simultaneously with the integration of the electrons trajectory through fields provided by a global magnetosphere model. We accomplish this through the combination of four separate modules. A schematic diagram summarizing the coupling between the modules is shown in Figure 1. The Multiscale Atmosphere Geospace Environment (MAGE) global geospace model provides accurate evolution of the storm-

time electromagnetic fields and plasmaspheric density. The Conservative Hamiltonian Integrator for Magnetospheric Particles (CHIMP) test-particle model provides an accurate description of storm-time electron transport and loss. An empirical wave model characterizes chorus wave power as a function of location, geomagnetic activity, and frequency, within the simulation. Finally, a wave-particle interaction module incorporates local pitch angle scattering and energy diffusion due to resonance with the electromagnetic waves.

2.1 Global Geospace Model

The MAGE model combines the Grid Agnostic MHD for Extended Research Application (GAMERA) global magnetohydrodynamic (MHD) model (Zhang et al., 2019; Sorathia et al., 2020), and its integrated ionospheric model, REMIX (Merkin & Lyon, 2010), with the Rice Convection Model (RCM) in the inner magnetosphere (Toffoletto et al., 2003). The MAGE model was designed to capture critical mesoscale features that regulate storm-time geospace dynamics (Sorathia et al., 2020; Lin et al., 2021; Sorathia et al., 2021; Pham et al., 2022). For a description of the MAGE model and its components, see both Sorathia et al. (2023, submitted) and Sciola et al. (2023). The cold plasma density controls the distribution of different wave populations in the inner magnetosphere (Malaspina et al., 2016), as well as the resonant interactions with the waves themselves (Summers et al., 1998; Summers, 2005). In the MAGE model, the plasmaspheric mass is dynamically evolved as a cold, formally zero energy, fluid by the RCM (Lin et al., 2021). The plasmaspheric density in the inner magnetosphere is initialized with the empirical global core plasma model (Gallagher et al., 2000) and the observed Kp index at the start of the event. The plasmasphere is then evolved using the same self-consistent electrostatic potential computed by REMIX. The mass of the cold plasmasphere is ingested back into the global magnetosphere simulation along with the ring current mass and pressure (Pembroke et al., 2012; Lin et al., 2021). The plasmaspheric density is the field-line averaged value and is assumed to be constant along the field-line. As the convective electric field erodes the plasmasphere, the plasmaspheric mass is refilled, using an empirical model (Denton et al., 2012) derived from radio emissions observed by the IMAGE spacecraft. The refilling time of the plasmasphere is on the order of several days. Therefore, refilling is more important during lower activity levels having less impact during shorter time periods associated with geomagnetic storms, which we are interested in modeling in this work.

2.2 Test-Particle Simulation

We model the radiation belts with an ensemble of test particles, ranging in energies and pitch angles that fully capture the radiation belt population. A test particle treatment is valid for radiation belt dynamics, since relativistic electrons make a negligible contribution to the plasma pressure, and consequently, do not produce feedback on the fields that drive their motion. CHIMP is a particle integrator, fully integrated to work with the complex 3D grid geometries used by GAMERA. CHIMP computes the trajectories of particles through the 3D, time-dependent electromagnetic fields generated by the MAGE model. CHIMP is capable of calculating the trajectories using either the relativistic Lorentz equations of motion or a relativistic Hamiltonian formulation of the guiding center trajectories (Sorathia et al., 2018; Sorathia et al., 2019). Also available within CHIMP is a mixed integrator that alternates between a guiding center formulation and the Lorentz trajectory. The ratio of the particle gyroradius to local magnetic field length scale is used as the criterion to switch between the two formulations. The test particle distribution is converted into a PSD by assigning each particle a weight. The particle weight relates the number of real electrons each test-particle acts as a proxy for and is calculated to match an initial, specified PSD. The time evolution of PSD is computed on a discretized phase space grid, using known weights and updated test particle positions. For more details on the calculation, see appendix A2 of Sorathia et al. (2018).

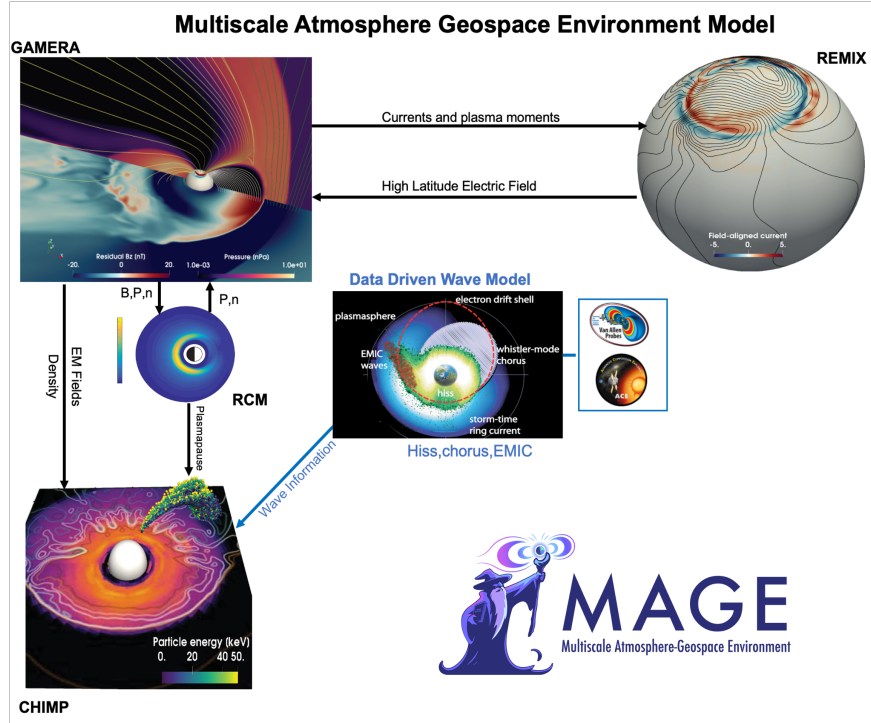


Figure 1. System architecture diagram showing the flow of information between the component modules in the simulation when wave particle interactions are included.

2.3 Data-Derived Wave Module

Specification of the properties of all relevant wave modes throughout the inner magnetosphere is required to assess the net effect of local wave-particle interactions on electron intensities. Electromagnetic wave-modes that exhibit cyclotron resonance with energetic electrons in the radiation belts, such as whistler waves, are driven by kinetic processes and, therefore, are not captured by isotropic single fluid MHD models. Most plasma waves identified as important to sculpting radiation belt population have amplitudes much smaller than the background fields. Therefore, one can consider the wave mechanisms independently from other processes. Wave occurrence rates and power depend on the solar wind and geomagnetic activity. To derive the global wave field specification from in situ spacecraft measurements, previous studies produced statistically-averaged 2D maps (L -MLT and/or L -MLAT) of wave amplitudes binned by a geomagnetic activity index (Kp or AE) of whistler-mode hiss (e.g., W. Li et al., 2015), and chorus (e.g., W. Li et al., 2016; Agapitov et al., 2018; Wang et al., 2019; Meredith et al., 2020) waves.

In this paper we use a slightly different approach to specify lower band chorus waves that enables a physically consistent integration of the data-derived wave power distributions into dynamically varying inner magnetosphere as described by the MAGE model (see Appendix A). The wave model is constructed based on the Van Allen Probes wave data over the entire mission period and supplies lower band chorus amplitudes as a function of L , MLT, MLAT, and the SuperMAG SML* index. The SML index is analogous to the AL index and is indicative of the level of substorm activity. SML* is defined as the minimum SML index during the preceding three hours (Gjerloev, 2012; Newell & Gjerloev, 2012, 2014). An example of the integration of the wave module into MAGE and CHIMP is depicted in Figure 2 for four different times throughout the simulation. Chorus waves are well organized by distance relative to the plasmopause, dL_{pp} (Malaspina et al., 2016). To maintain physical consistency between the distribution of waves and the plasma environment within the global model, lower band chorus waves from the empirical wave model are ingested into the simulation relative to the modeled plasmopause location. To this end, the wave distribution was re-parameterized according to dL_{pp} . The plasmopause in the empirical model is taken to be the average of the minimum L -shell where chorus waves are present in each MLT bin. The time-dependent plasmopause boundary passed from the RCM module is used to rescale the obtained wave distributions onto the model domain for each step of the global magnetosphere simulation. Here, we define the plasmopause location in the MAGE model to be where the plasma density reaches 100 cm^{-3} , as in Ripoll et al. (2022). We additionally only include waves within the inner magnetosphere, without taking into account waves in the magnetosheath.

2.4 Wave-Particle Interaction Module

Local acceleration and scattering of electrons through wave-particle interactions is computed from the Fokker-Planck diffusion equation via an SDE. The diffusion equation utilizes analytical expressions for the quasi-linear diffusion coefficients derived by Summers (2005). These coefficients are local, calculated at the particles position, and assume chorus wave propagation parallel to the magnetic field. Lower band chorus waves are predominantly quasi field-aligned, especially during geomagnetically active times (W. Li et al., 2016). The parallel propagation assumption greatly reduces the complexity of the problem, making the inclusion into test particle simulations more tractable. Chorus waves typically have small wave normal angles ($< 20^\circ$), however, large values have also been measured (e.g., W. Li et al., 2011). Shprits et al. (2006) showed that the bounce-averaged diffusion coefficients for lower-band chorus interaction with hundreds of keV to a few MeV electrons were dominated by the resonant harmonic associated with parallel propagating waves. Restricting our consideration to parallel propagating waves, therefore, should not significantly affect the analysis of electron acceleration up to the energies of a few MeV.

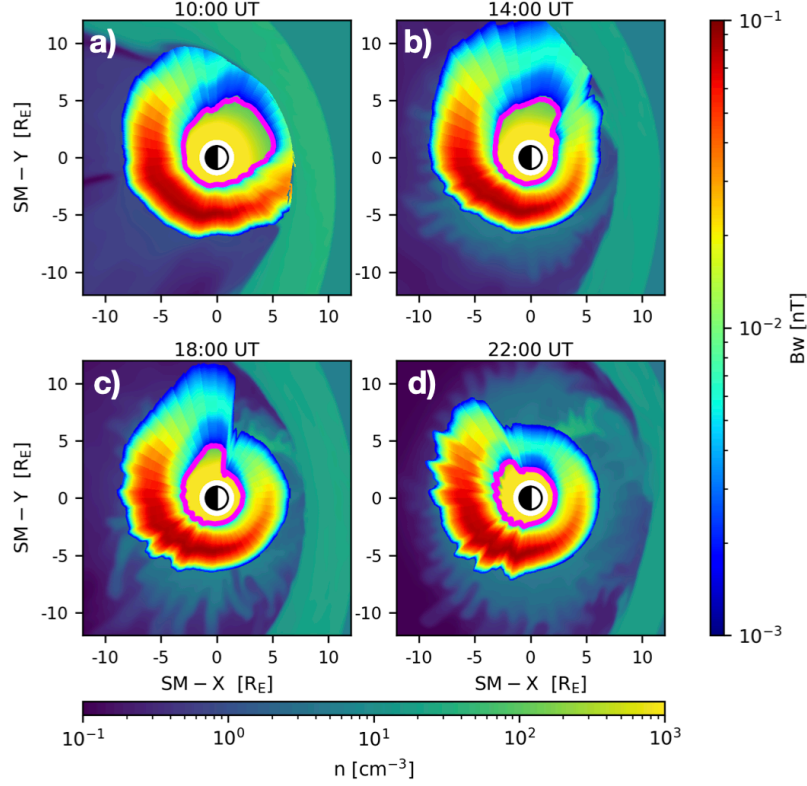


Figure 2. Storm-time evolution of the plasmasphere and resulting chorus wave location throughout the main phase of the 17 March 2013 event. Snapshots in the equatorial plane of the MHD plasma density and ingested chorus wave amplitude at four times, each four hours apart. The magenta line denotes the location of the plasmapause in the model, defined by a plasma density of $n=100 \text{ cm}^{-3}$.

The diffusion coefficients depend on the background magnetic field and density, see equation B6. The magnetic field and density are taken directly from the magnetosphere model at the particle's location. Therefore, local acceleration changes dynamically along electron trajectories as they propagate through the background plasma with varying density and ambient magnetic field magnitude.

The implementation of wave-particle interactions is general and can be applied to multiple wave modes. These wave modes can be considered separately, or in orchestra, to quantify the effect on the system. A full description of the wave-particle interaction module included within CHIMP is provided in Appendix B.

3 17 March 2013 Storm Case Study

In this paper we applied our newly developed model to the March 17 2013 storm. The storm was caused by the interplanetary shock driven by a coronal mass ejection that struck the Earth at 6 UT, causing an initial rapid drop out of the radiation belt flux likely attributed to particle loss through the magnetopause (e.g., Baker et al., 2014). A rapid enhancement of electron fluxes for energies below a few MeV followed the dropout, while multi-MeV energies gradually increased in flux over the next ten hours. Fluxes eventually exceeded the pre-storm values by more than an order of magnitude (Baker et al., 2014; W. Li et al., 2014; Ukhorskiy et al., 2015). A minimum storm-time SYM-H index of ≈ -130 nT was reached just prior to 21 UT under continuous southward B_Z driving. Chorus wave activity was observed directly by both Van Allen Probes (RBSP) A and B, as well as indirectly inferred from POES precipitation measurements. Waves occurred during the entire period of enhancement from 10 UT until midnight (W. Li et al., 2014).

The global magnetosphere simulation used in this study is described in detail by Sorathia et al. (2023, submitted). Sorathia et al. (2023, submitted) also includes a data-model comparison of the SuperMAG indices. In this simulation, GAMERA's modeling domain extended from $25 R_E$ at the subsolar point to $300 R_E$ down the magnetotail and had a spherical inner boundary at $1.5 R_E$. GAMERA utilizes a warped spherical grid with $192 \times 192 \times 256$ cells in the radial, polar, and azimuthal directions. This grid is $2\times$ more refined in each dimension than the earlier LFM simulation of the same event (Wiltberger et al., 2017; Sorathia et al., 2018). The REMIX solver for the electrostatic potential used a uniform grid with 0.5-degree resolution in both latitude and longitude. The low latitude boundary of the REMIX grid was set by the dipole mapping of the MHD inner boundary to the ionosphere. The REMIX solution was coupled with GAMERA every 5 seconds. The spatial domain of the RCM grid had a resolution of $0.25^\circ \times 1^\circ$ in latitude and longitude, respectively. In this work, we used 115 energy channels that consisted of 29 channels for electrons, 85 channels for protons, and a single zero-energy channel for the cold plasmasphere. At geosynchronous orbit, this corresponds to peak energies of ≈ 10 keV for electrons and ≈ 100 keV for protons. The updated plasma density and pressure from RCM were ingested into MHD solution at a frequency set at a cadence of 10 seconds.

The MAGE model was driven by solar wind data taken from the OMNI database at 1 minute resolution. Data gaps were linearly interpolated to provide continuous boundary conditions for the simulation. The solar F10.7-cm flux index used for the ionospheric conductance was set to 124.5, the daily flux density during the event, taken from the OMNI data set. The magnetosphere simulation started at 00 UT on 17 March 2013 and was preconditioned with real solar wind for 6 hours before the sudden storm commencement. The simulation was run for a total of 30 hours, encompassing the entire main phase of the storm and several hours into the recovery phase. The three-dimensional electromagnetic fields and plasma solution generated by the simulation were saved at a cadence of 30 seconds.

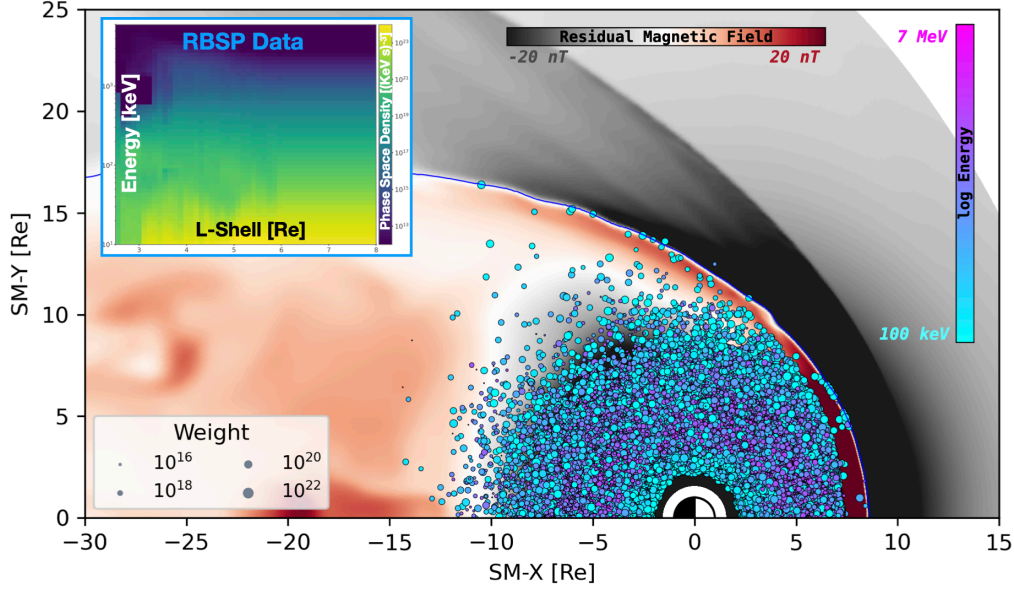


Figure 3. An overview of the global magnetosphere and test particle simulation in the SM equatorial plane at 13:20 UT on 17 March 2013. The figure shows color contours of the residual magnetic field in the equatorial plane, with the dipole field removed. Regions where the field is compressed are in red. Test particle locations are projected along magnetic field lines to the equatorial plane. The size of each marker corresponds to the weight of the particle. The initial PSD from the Van Allen Probes used to weight the test particles is provided in the upper left inset. The simulated period relative to the observed SYM-H index is given in the bottom panel.

We utilized the guiding center formalism to compute the test-particle trajectories. Test particles were initiated and integrated on a subdomain of the full MHD grid within a spherical region defined by a radius of $20 R_E$ and centered at the origin. The magnetic field was assumed to be a dipole below the $1.5 R_E$ inner boundary of the MHD grid. Test particle trajectories were solved down to an altitude of $1.05 R_E$. Particles that exit the outer boundary of the domain or do not bounce before $1.05 R_E$ were considered lost from the system.

To isolate the impact of local chorus acceleration on the radiation belts, we removed the effect of injections (Z. Li et al., 2015; Sorathia et al., 2018) and included only the evolution of the initial radiation belt population. We refer to the modeled population as the pre-existing belt. The pre-existing particle population was initialized in the SM equatorial plane, $Z=0$, at 10 UT. The particles were uniformly distributed in MLT and pitch angle, between $L = 2.5$ and $L = 8$ with energies ranging from 50 keV to 5 MeV. In total, 2 million particles were evolved for 14 hours throughout the entire acceleration period from 10 UT until midnight on 18 March 2013. Figure 3 provides an overview of the test particle simulations. The simulated period of the radiation belts relative to the

observed SYM-H index is also provided in the bottom panel of Figure 3 for additional context.

The pre-event PSD used to weight the test particles was derived from Van Allen Probes data, using the ECT combined data product provided by Boyd et al. (2019). The PSD was taken over the outbound orbit between 10 UT and 14 UT on 17 March 2013, similar to Ma et al. (2018). We computed the PSD on a grid as a function of energy and L -shell. It spanned energies from 10 keV to 6 MeV and L -shell coverage from $2.5 R_E$ to $8 R_E$, with 55×50 cells in each dimension respectively. PSD was averaged over the measurements in each bin from both RBSP A and B. For $L > 6$, the PSD was set to match the value at geosynchronous orbit. This approximation did not impact the conclusions of this paper; particles initialized at $L > 6$ were quickly lost to the magnetopause due to the compression at the beginning of the simulation and therefore do not contribute to the final PSD at the end of the main phase. The initial PSD from RBSP-A and B used to weight the test particles is given in the inset of the upper panel of Figure 3. The time-evolved PSD was calculated on a discretized phase space specified in the SM equatorial plane and discretized by L , azimuthal angle (ϕ), equatorial pitch angle (α_{eq}), and particle kinetic energy (K). L and ϕ were set for each particle using their equatorial crossing point. The phase space domain for the results shown in this work is given by $\Gamma(L, \phi, \alpha_{eq}, K) = [2.5, 10] \times [0, 2\pi] \times [0, \pi] \times [50 \text{ keV}, 7 \text{ MeV}]$. The grid cells were linearly spaced for L , ϕ and α_{eq} and were logarithmic in energy. The number of cells set in each dimension was set to (30, 24, 9, 30), respectively.

To quantify local scattering and acceleration from lower band chorus wave, we performed two test particle simulations. Both simulations evolved initially identical radiation belt populations through the time varying electromagnetic fields from the MAGE model. The data-derived wave module combined with the wave-particle interaction module were incorporated into one simulation and were not included in the other. The location of the lower band chorus waves from the empirical wave model was evolved in time according to the simulated plasmopause location and the observed SML^* index during the event, provided by the SuperMAG collaboration (Gjerloev, 2012; Newell & Gjerloev, 2012, 2014).

4 Results

4.1 The Role of Storm-Time Magnetic Field and Density on Wave-Particle Interactions

The storm-time evolution of the magnetic field and cold plasma density can alter the efficiency of wave-particle interactions by changing the magnitude of the wave-particle interactions and the energies electrons resonate at. To assess how the evolution of the background plasma alters wave-particle interactions, we performed bounce averaging of the local diffusion coefficients. Here, we focused on effects longer than a typical bounce period of electrons. The full calculation of the bounce-averaged diffusion coefficients is provided in Appendix C. $\langle D_{\alpha\alpha} \rangle$, $\langle D_{\alpha p} \rangle$ and $\langle D_{pp} \rangle$ were calculated as a function of energy and α_{eq} . The calculations were performed on a uniform grid with half an hour resolution in MLT and $0.25L$ resolution in L between $2.5 < L < 10$. The calculation used the magnetic field and density directly from the MAGE model at the specified time to provide a snapshot of particle diffusion. We note that, while bounce-averaging the diffusion coefficients illustrates the connection to the background plasma conditions, the local diffusion coefficients were used to solve each individual resonant interaction in Section 2.4.

Figure 4 presents $\langle D_{\alpha\alpha} \rangle$ for 2 MeV and 100 keV electrons, each with $\alpha_{eq} = 55^\circ$, at four time instances spread uniformly through the main phase of the storm. The selected times are identical to those used in Figure 2 that details the storm-time evolution

of the modeled plasmasphere and the resultant chorus wave power distribution. $\langle D_{\alpha\alpha} \rangle$ is zero in the blank regions of Figure 4e-4l. These locations denote where either no chorus waves were present or no resonance occurred along the electron bounce. For electrons in resonance with lower band chorus waves at frequencies significantly lower than the plasma frequency, the minimum resonant energy is $E_{min} = E_C (|\Omega_e|/\omega) (1 - \omega/|\Omega_e|)^3$, where Ω_e is the electron gyrofrequency and ω is the resonant wave frequency (e.g., equation 2.19 of Kennel & Petschek, 1966). E_C is the characteristic energy for cyclotron interactions and is defined as $E_C = B^2/8\pi N \propto f_{ce}^2/f_{pe}^2$. Hence, variations in both the magnetic field and the cold plasma density can strongly affect the resonance energy of wave-particle interactions. The top row of Figure 4 shows the evolution of the cold plasma parameter, f_{pe}/f_{ce} , in the equatorial plane during the main phase of the storm. While the magnetic field also exhibited a significant non-dipolar structure, most of the variation in f_{pe}/f_{ce} was driven by the cold plasma density.

Increased storm-time convection erodes the nightside plasmasphere and forms the plasmaspheric plume (Grebowsky, 1970; Foster & Burke, 2002; Borovsky & Denton, 2006; Darrouzet et al., 2009). This can be seen in the increase in f_{pe}/f_{ce} in Figure 4a at 10 UT, as the cold, dense mass extended to the dayside magnetopause. Several hours into the storm, continued enhanced convection further eroded the plume causing it to narrow in MLT, shown in Figure 4b. In Figure 4c and 4d, the plume ultimately began to rotate as convection decreased. The modeled plume behavior qualitatively matches observations during geomagnetically active periods (Goldstein & Sandel, 2005). This dynamic evolution of the plasmaspheric plume, combined with the reduction of the magnetic field due to the ring current, has major implications for wave-particle interactions. The extension of the plume to larger L -shells caused an increase in the plasma frequency and lowered the minimum electron energy in resonance with the waves (Kennel & Petschek, 1966). The plume enabled lower energy electrons to be scattered into the loss cone, increasing the precipitation in those regions, as previously reported by observations (W. Li & Hudson, 2019). However, as seen by the absence of $\langle D_{\alpha\alpha} \rangle$ in Figure 4e-4l, the higher ratio of f_{pe}/f_{ce} in the plume shifted the resonance region to lower energies such that ≥ 100 keV electrons do not exhibit resonance with lower band chorus waves.

The increased density also significantly impacts the magnitude of the scattering and energization resulting from the interaction (Summers et al., 1998; Summers, 2005). Continuing storm-time convection significantly eroded the dayside plasmasphere. The erosion formed a low-density trough. This reduced the ratio of f_{pe}/f_{ce} just outside the plasmopause, seen in Figure 4b-4d. The trough initially formed on the dawnside at pre-noon before extending to the dayside. The density depletion, in combination with the reduced magnetic field strength from the ring current, reduced this f_{pe}/f_{ce} to ~ 0.1 at very low L -shells from 14 UT to 22 UT. The low f_{pe}/f_{ce} shifted the resonance zone to higher energies to include multi-MeV electrons. Therefore, despite having lower wave amplitudes in this region (see Figure 2), the scattering and acceleration for 2 MeV electrons was enhanced. This is exhibited by the increase in $\langle D_{\alpha\alpha} \rangle$ in the pre-noon sector just outside the plasmopause in Figure 4f-4h. In contrast, $\langle D_{\alpha\alpha} \rangle$ for 100 keV electrons was only weakly affected by the density erosion on the dayside. Instead, the diffusion rates remained the largest in the post-midnight to dawn sectors where the wave amplitudes were the largest, shown in Figure 4i-4l.

4.2 Electron Flux Enhancements

Figure 5 presents the evolution of the radiation belt intensity, $j = p^2 f_{PSD}$. The intensity is calculated by averaging the PSD over pitch angle, gyrophase, and MLT. Figure 5 compares the initial distribution of j as a function of energy and radius to the average intensity at the end of both simulations, when an enhancement of multi-MeV electrons was observed by the Van Allen Probes. Magnetopause losses are most apparent when comparing the average intensity of the initial distribution in Figure 5a to the av-

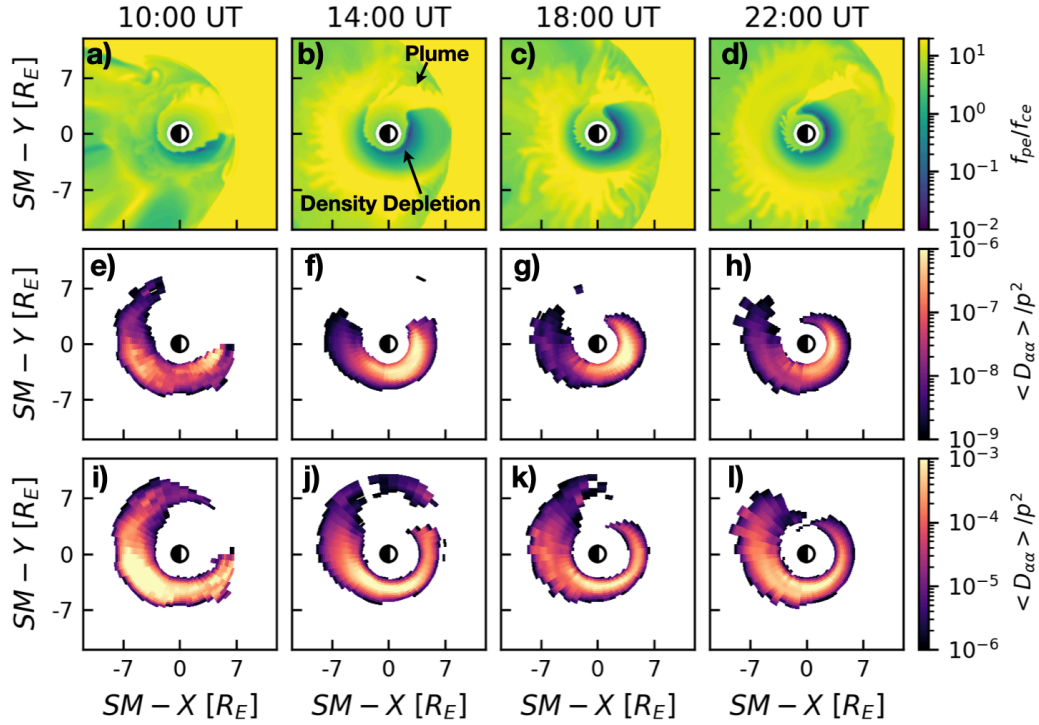


Figure 4. Overview of the influence of the background plasma conditions on quasi-linear diffusion coefficients. The times selected match those shown in Figure 2. The cold plasma parameter, f_{pe}/f_{ce} , in the equatorial plane is shown in the top row. The middle and bottom rows show $\langle D_{\alpha\alpha} \rangle$ due to chorus waves, in units of s^{-1} , for 2 MeV and 100 keV electrons, respectively, both with $\alpha_{eq} = 55^\circ$. $\langle D_{\alpha\alpha} \rangle$ is calculated using the instantaneous magnetic field, density, wave amplitudes and locations from the magnetosphere and empirical wave models.

erage intensity at the end of the simulation in Figure 5b. As noted in Section 4.3, only magnetopause loss occurred in the simulation that lacked scattering from wave-particle interactions. Loss of electrons through the magnetopause boundary resulted in the reduction in the average intensity by an order of magnitude for all energies at $R > 4 R_E$, shown in Figure 5b.

By the end of the main phase of the storm, the Van Allen Probes observed enhancement of relativistic radiation belt fluxes by an order of magnitude relative to pre-storm levels. (Baker et al., 2014; W. Li et al., 2014; Ukhorskiy et al., 2015). Through comparison of Figure 5a and 5b, we show that acceleration via transport alone did not produce a significant enhancement in the outer radiation belt intensity at MeV energies, agreeing with the previous results of Sorathia et al. (2018). Furthermore, in Figure 5b, there is no distinguishable increase in average intensity for ≥ 1 MeV electrons below $R < 4 R_E$ relative to the initial distribution, while, at larger distances, a reduction in average intensity occurred. Figure 5c and 5d show, however, that local acceleration from lower band chorus waves did accelerate electrons to MeV energies, as shown by previous studies (W. Li et al., 2014; Ma et al., 2018; Chan et al., 2023). Additional acceleration from wave-particle interactions increased the average intensity by up to three orders of magnitudes for multi-MeV electrons at $R > 2 R_E$. This suggests that electron resonance with chorus waves is a likely candidate for the additional source needed to capture the multi-MeV enhancement at the end of the storm main phase.

The enhancement arose due to the acceleration of radiation belt electrons with initial energies below 1 MeV to multi-MeV energies. The simulation was restricted to the evolution of the pre-existing belt and did not contain electron injections from the central plasma sheet that supply the continuous source of electrons between 50-100s, as shown by Sorathia et al. (2018). Consequently, there was a depletion in electrons below ~ 500 keV, as shown in Figure 5d.

Figure 6 presents the equatorial pitch angle and energy distribution of MLT-averaged PSD at the peak of the outer belt average intensity at $L = 3.7$. We compare the initial PSD distribution to the PSD from the end of both simulations with and without wave-particle interactions. Shown in Figure 6d, there is a reduction in the ratio of the PSD for the lowest equatorial pitch angles between the simulation including wave-particle interactions and the simulation with only radial transport effects. This difference is attributed to diffusion into the loss cone caused by chorus wave resonance with subsequent particle loss into the atmosphere. Wave-particle interactions also caused the pitch angle distribution to become more anisotropic, which is indicative of electron acceleration by their resonant interaction with the waves. Due to the absence of a parallel electric field, resonance with parallel propagating waves conserves the particle kinetic energy in the frame moving with the phase velocity wave. Particles are therefore constrained to diffuse along resonant phase-space curves that uniquely determine the change in momentum from a given change in pitch angle (Summers et al., 1998). For a given resonant diffusion curve, particles gain energy as they are scattered to larger equatorial pitch angles (Kennel & Petschek, 1966). This leads to a pitch angle distribution at higher energies that is initially more equatorial, forming a pancake distribution at multi-MeV energies, similar to what we see in Figure 6c.

In both simulations with and without wave-particle interactions, there was a peak in the PSD at $\alpha_{eq} \sim 90$ deg for energies below ~ 400 keV, seen in Figure 6b and 6c. This feature is attributed to the lack of resonance of these electrons with lower band chorus waves. Therefore, the electrons have had few opportunities to be scattered out of these PSD cells from wave-particle interactions. If present, the higher frequency of upper band chorus waves would extend the resonance region to include the electrons near $\alpha_{eq} = 90$ deg below ~ 400 keV and would enable scattering of this population of electrons.

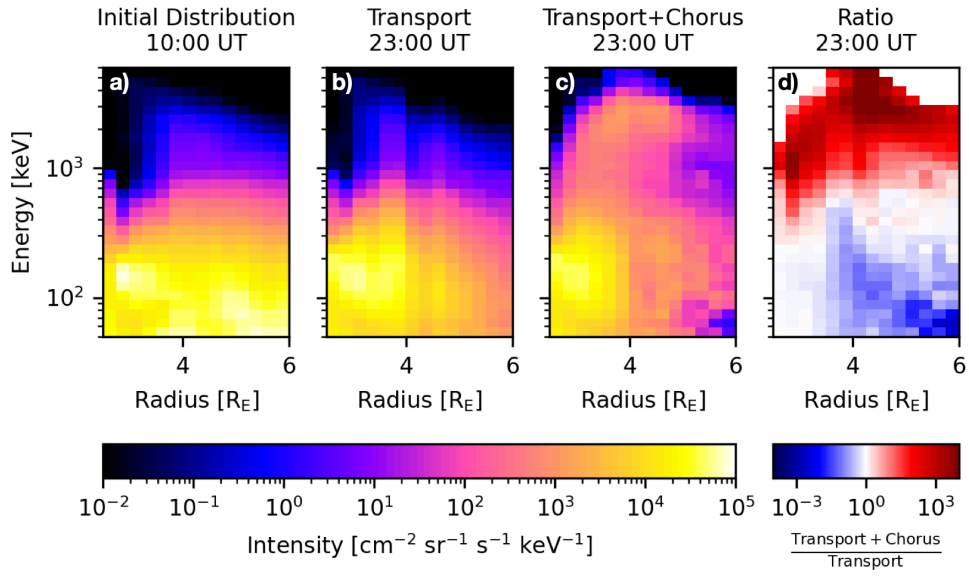


Figure 5. MLT-averaged intensity as a function of energy and radial distance. The initial distribution is shown on the left most panel. The average intensity at 23 UT for the cases with transport only and when wave-particle interactions were included are presented in the middle two panels with their ratio provided in the right most panel.

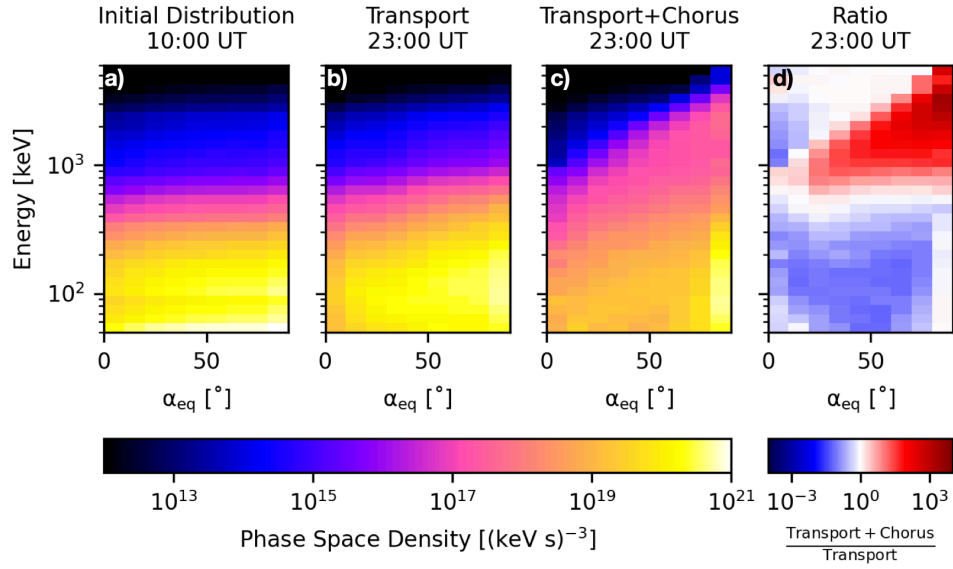


Figure 6. Similar to Figure 5, showing the MLT-averaged phase space density at $L = 3.7$ as a function of energy and equatorial pitch angle.

The purpose of this investigation is to compare the impact of wave-particle interactions in the model to the stand-alone radial transport simulation. Due to this and the exclusion of injections, we do not directly compare the simulated average intensity to RBSP-A measurements. The full data-model comparison is left for a future paper that will include the full range of diffusive and non-diffusive processes. Figure 7 presents a quantitative comparison of the intensities between the simulations when wave-particle interactions were included, shown in green, and when they were not, shown in orange. It shows "synthetic measurements" at RBSP-A, i.e., the average electron intensity extracted from test particle simulations computed along the spacecraft orbit from the time-evolution of the simulated PSD. The modeled average intensity in Figure 5 incorporates contributions from all particles along a given field line that maps from the spacecraft location to the corresponding PSD cell in the equatorial plane. To account for the fraction of electrons that mirror before reaching the spacecraft location, we performed field line tracing through the time-dependent global magnetosphere model to extract the equatorial projection of the spacecraft position along with the local and equatorial magnetic field strength. We further assumed the pitch angle distribution has a $\sin^n(\alpha)$ dependence to determine the attenuation factor, J_{scl} , calculated as

$$J_{scl} = \frac{\int_0^{\alpha_M} \sin^n(\alpha) d\alpha}{\int_0^\pi \sin^n(\alpha) d\alpha} \quad (1)$$

where α_M is the largest equatorial pitch angle that can be measured at the spacecraft location. In this work, we set $n = 2$, as done in Sorathia et al. (2018). The average intensities plotted in Figure 7 are energy weighted averages across the selected MagEIS MeV energy channels (Blake et al., 2013).

The comparison in Figure 7 between the simulations with and without wave-particle interactions highlights the importance of local electron acceleration by lower band chorus waves. The inclusion of local acceleration resulted in an order of magnitude or more enhancement of the radiation belt intensity relative to the simulation when only transport effects were included. Local wave-particle interactions led to a rapid increase in the radiation belt intensity within the first few hours, while RBSP-A was within the core of the outer belt, shown by the green curve in Figure 7. The increase was primarily due to electrons with large initial equatorial pitch angles ($\alpha_{eq} > 60^\circ$). The bounce motion of these electrons is entirely contained within the magnetic latitudes where waves were present. This enabled continuous resonance and acceleration to higher energies. The apogee of the RBSP-A orbit was in the magnetotail, near midnight, during this event. Seen in Figure 4b, the cold plasma parameter, f_{pe}/f_{ce} , increased as RBSP-A approached apogee around 15:00 UT. The acceleration at the highest energies was therefore reduced despite wave amplitudes being large at those L -shells. This decrease in $\langle D_{\alpha\alpha} \rangle$ in the magnetotail at midnight for MeV electrons is shown in Figure 4f. By the time of the second outbound orbit, starting at 20 UT, continuous wave-particle interactions caused a several decade enhancement, relative to the previous apogee at 15 UT, of the ≥ 1 MeV average intensity across the entire outer belt up to geosynchronous orbit. In the simulation with wave-particle interactions, green curve in Figure 7, the enhancement of the electron intensity between the first and second apogees was not as significant at 1 MeV as it was at higher energies. This can be attributed to a combined effect of 1 MeV electrons being accelerated to multi-MeV energies and the absence of electron injections to replenish to 1 MeV population. Through comparison to the simulation when only transport effects were included, Figure 7 shows that the inclusion of local acceleration due to resonance with lower band chorus waves resulted in an order of magnitude or more enhancement of the radiation belt intensity at the end of the main phase.

It should be noted that chorus waves in the data-derived wave model, described in Section 2.3 and Appendix A, were distributed within 45° magnetic latitude throughout all MLT sectors in order to mimic pitch-angle scattering by oblique chorus waves. Statistically, lower band chorus waves are observed below 15° in the evening to dawn sec-

tor, below 30° in the dawn to afternoon sector, and up to 45° on the dayside (e.g., Agapitov et al., 2018; Meredith et al., 2012). While the wave amplitude used in the model decreased with magnetic latitude (equation A1), the assumption that lower band chorus waves were contained up to 45° in all MLT sectors may cause the model to overestimate the amount of local scattering and acceleration of relativistic electrons that occurred when compared to a more realistic MLT distribution of the latitudinal extent of the waves, if the chorus activity is dominated by parallel propagating waves. Calibration of the wave amplitude as a function of magnetic latitude and MLT is left for the future paper containing the full data-model comparison with RBSP observations.

4.3 Storm-Time Loss Processes

Figure 8 presents an overview of the losses throughout the simulation that includes chorus wave-particle interactions. There are two possible mechanisms responsible for radiation belt losses. Electrons either escape through the magnetopause due to rapid changes in configuration or via precipitation into the atmosphere. In our model simulations, electrons were considered to precipitate into the atmosphere if they did not bounce before reaching the spherical inner boundary of CHIMP, set at $1.05 R_E$. The test particles were considered to be lost through the magnetopause if they crossed from closed to open field lines. To identify magnetopause crossings, field line tracing was performed for every test particle at each simulation step. A field line was defined to be magnetospheric, open, or interplanetary magnetic field (IMF), if both, one, or none of its foot points map to the ionosphere, respectively. Any open-closed boundary transition was identified as a loss event without making a distinction between transitions to open and to IMF field lines, as was previously done in Sorathia et al. (2017).

Electrons did not precipitate and were lost only through the magnetopause when only radial transport effects were taken into account in the test particle simulation. Even in the presence of wave-particle interactions with lower-band chorus, the majority of electrons were lost through the magnetopause. Magnetopause loss contributed to $\sim 60\%$ of total losses, or $\sim 40\%$ of the initial radiation belt, shown by the blue curve in Figure 8. This confirms previous simulation results of storm-time dropouts of the radiation belt (Ukhorskiy et al., 2015; Sorathia et al., 2018). The largest increases in magnetopause losses occurred in rapid increments as the dynamic pressure of the solar wind quickly compressed the magnetosphere. The simulation, without scattering from wave-particle interactions, had a similar magnetopause loss profile to the blue curve in Figure 8, however, $\sim 46\%$ of the initial belt was lost. The difference between the simulations potentially can be attributed to electrons lost to precipitation when resonant interactions were included that might otherwise have been lost through the magnetopause later in the storm.

When compared to the model where only transport was included, wave-driven precipitation increased the total loss by $\sim 14\%$ during the 14 hour simulated period. The precipitation accounted for $\sim 1/3$ of the total loss when both transport and pitch-angle scattering were present, denoted by the red curve in Figure 8. The precipitation loss rate also decreased over time. This is caused by the reduction in diffusive scattering rates as electrons are accelerated to higher energies. Therefore, fewer electrons were scattered into the loss cone as a function of time.

While the latitudinal distribution of the waves used within the wave model may result in an overestimation of the precipitation, our simulations did not include either the initial dropout event at 6 UT due to the shock arrival, or electron injections throughout the storm main phase. Injections would have provided an additional source that could either be scattered into the loss cone or immediately lost to the magnetopause if they are not on trapped orbits. Even without an additional particle source, we found that that precipitation can still be a significant component of radiation belt loss when wave activity is high.

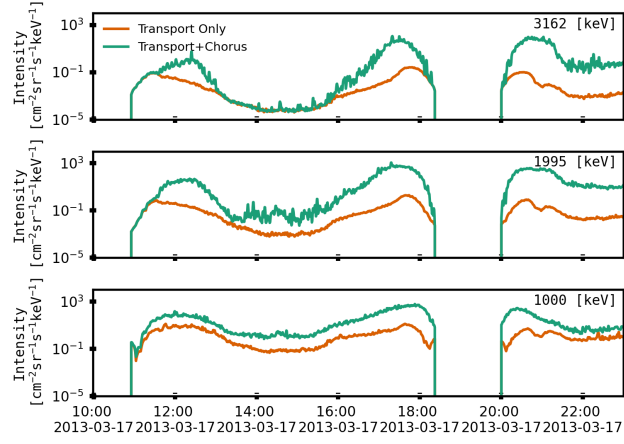


Figure 7. Comparison of model-predicted average intensity at RBSP-A when local wave-particle interactions were included (green) and when they were not (orange) at selected MeV energy channels.

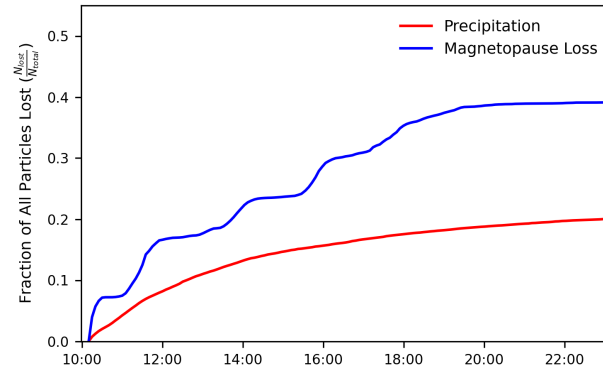


Figure 8. Overview of the evolution radiation belt losses throughout the simulation. The blue and red curves denote the fraction of the electrons, relative to the total number of electrons initially present, that were lost either through the magnetopause or precipitated into the atmosphere, respectively. Particles lost to precipitation was determined if they did not bounce before reaching our inner boundary of $1.05 R_E$.

Figure 9 presents the number flux, mean energy, and energy flux of precipitating electrons in the ionosphere. The precipitation shows the combined contribution from both hemispheres and was accumulated over the entire test particle simulation. The majority of precipitation, both in terms of number flux and energy flux, occurred in the post-midnight to dawn sector where wave amplitudes were the largest, as shown in Figure 2. The precipitation in this region comprised mostly of electrons with energies ≤ 200 keV, shown in the middle panel of Figure 9. This is consistent with the corresponding $\langle D_{\alpha\alpha} \rangle$ for 100 keV electrons in the bottom row of Figure 4. The shift in resonant scattering of higher energy electrons to lower L -shells in the pre-noon sectors due to erosion of the plasmasphere is also apparent in the mean energy of the precipitating flux. Shown in the middle panel of Figure 9, the mean energy of precipitation increased with increasing co-latitude in both the pre-noon sector and towards the dayside. This highlights the strong dependence of wave-particle interactions on the evolution of the background plasma conditions.

5 Discussion and Conclusions

Understanding the outer electron radiation belt is a system level problem of geospace. This is especially true during geomagnetic storms where rapid variability of the radiation belt fluxes is prevalent. Realistic representation of storm-time magnetospheric electrodynamics is critical for capturing the dynamic response of the outer radiation belt intensity. A physically consistent solution of the outer radiation belt within the global magnetosphere is important to capturing key acceleration and loss processes, such as injections from the plasma sheet, magnetopause losses, and wave-particle interactions. A flexible, modular framework enables global radiation belt models to isolate the effects of each mechanism, including the balance between diffusive and non-diffusive processes that produce similar features, such as localized peaks in electron PSD (Kim et al., 2023).

In the present paper we presented a new model of the radiation belts that incorporates quasi-linear diffusion from resonant wave-particle interactions with whistler-mode chorus waves into our global magnetosphere and test particle model. The radiation belt model was driven solely by the upstream solar wind conditions, the solar F10.7-cm flux, and a data-derived specification of the chorus wave power. Pitch-angle scattering and acceleration from wave-particle interactions was computed using a time-forward SDE to solve the Fokker-Planck diffusion equation. The diffusion equation was solved simultaneously with the integration of electron trajectories through electromagnetic fields provided by the magnetosphere model and was based on analytical expressions for the *local* quasi-linear diffusion coefficients (Summers, 2005). The local diffusion coefficients were derived for cyclotron resonance with field-aligned electromagnetic waves and are calculated for each instance of resonant wave-particle interactions are computed. An empirical wave model was used to set the chorus wave amplitude as a function of location and geomagnetic activity. The chorus waves were dynamically ingested into the model based on the dynamically changing plasmapause location in the simulation. We used analytical expressions for the local diffusion coefficients that depend on the background magnetic field and cold plasma density. The background plasma conditions were taken directly from the magnetosphere model at the particle's location. Therefore, the diffusion coefficients varied throughout the storm as a function of time and location consistently with the plasma and the wave model.

While previous studies have applied SDEs to solve the Fokker-Planck equation (Tao et al., 2008; Zheng et al., 2014, 2021; Chan et al., 2023), this is the first study where pitch-angle scattering and acceleration have been included within a global magnetosphere and test-particle simulation using local quasi-linear diffusion rates that were physically consistent with the varying background plasma conditions. During geomagnetic storms, the enhanced convection electric field strongly impacts the evolution of the plasmasphere (e.g., Delzanno et al., 2021, and references therein). The plasmaspheric structure and dynam-

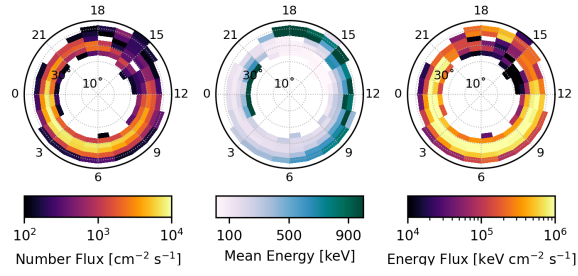


Figure 9. Number Flux (left), mean energy (middle), and energy flux (right) of precipitating electrons accrued over both hemispheres between 10 UT and 24 UT, shown as a function of colatitude and MLT. Regions with a number flux below $100 \text{ cm}^{-2} \text{s}^{-1}$ have been masked for clarity.

ics govern the generation and propagation of whistler mode waves prevalent in the inner magnetosphere, creating a strong MLT dependence during storm time. The cold plasma density not only influences the global distribution of the waves, but also plays a major role in mediating the resulting wave-particle interactions.

Additionally, we have shown that low values of the cold plasma density enable stronger scattering with multi-MeV electrons. Through scaling the density in the Sheeley et al. (2001) trough model, previous studies have established that very low values of the density accelerate electrons to ultra-relativistic energies (Allison et al., 2021). Using a physics-based model, we have demonstrated that lower density regions formed due to the plasmasphere erosion and efficiently accelerated electrons to multi-MeV energies. Furthermore, we have demonstrated that determining both the plasma trough density and plasma-pause location was important to regulating the presence of chorus waves, the energies of resonant electrons, and the magnitude of the scattering and energization. For that reason, consistently incorporating the storm-time evolution of the cold plasma density and chorus wave power is critical to capturing the dynamical effect of wave-particle interactions during all phases of geomagnetic storms.

We performed a case study of the enhancement of the outer radiation belt during the 17 March 2013 storm. RBSP PSD data was used as the initial condition to set the electron fluxes. To isolate the impact of the chorus waves, we simplified the simulation and neglected electron injections from the tail (Sorathia et al., 2018). We evaluated identical radiation belt distributions through two simulations, one included diffusion due to wave-particle interactions and the other did not. We showed that:

- Radial transport through accurate storm-time electromagnetic fields alone did not produce a significant flux enhancement at multi-MeV energies.
- Resonance with parallel propagating lower band chorus waves increased the modeled radiation belt intensity of > 1 MeV electrons by more than an order of magnitude at all L -shells within geosynchronous orbit.
- Evolution of the storm-time magnetic field and cold plasma density strongly affected the resonant energies of electrons and the magnitude of the resulting wave-particle interactions. The dynamic variation of the cold plasma density and magnetic field resulted in a strong energy and MLT dependence in pitch angle scattering, atmospheric precipitation, and energy diffusion throughout the event.
- Wave-particle interactions produced an anisotropic pitch angle distribution as the electrons were accelerated to multi-MeV energies.
- In the presence of waves, precipitation accounted for a third of the total loss of electrons from the outer belt.
- Precipitation consisted predominantly of 100s keV electrons, scattered into the loss cone on the dawnside where the chorus wave amplitudes were the largest.
- The mean energy of the precipitation increased to above 600 keV at low L -shells on the dayside due to a deep depletion of the cold plasma density caused by the erosion of the plasmasphere.

While the present simulation accounted for local wave-particle interactions only with lower band chorus waves, our approach for modeling wave-particle interactions is general. The technique can easily be extended to incorporate other wave modes that play an important role in scattering and energizing radiation belt electrons. Each additional wave mode can be modeled individually, or in concert with the others, to study their relative contribution. In addition, the algorithm can be modified to account for the oblique propagation of certain wave modes.

Our test-particle approach enables us to distinguish how electrons are accelerated, transported, and lost from the system. Global magnetosphere and test particle simulations now enable us to directly quantify the relative role local wave-particle interactions,

mesoscale particle injections, and large-scale radial transport via ULF resonance in governing radiation belt dynamics. Due to the physically consistent modeling of the magnetosphere and its impact on the radiation belts, we are now able to connect each mechanism directly back to the magnetic field and plasma conditions through which they are evolved on the time scales of seconds to hours that drive variability during geomagnetic storms.

6 Open Research

All RBSP-ECT data (Spence et al., 2013; Boyd et al., 2019) are publicly available at the Web site <http://www.RBSP-ect.1anl.gov/>. The OMNI data set are available at <https://cdaweb.gsfc.nasa.gov/index.html/> by selecting OMNI from the available spacecraft and then the 1-minute resolution data. Simulation data used to create the figures are available on Dropbox at <https://www.dropbox.com/scl/fo/7kzzww10geeajhmd9ltxr/h?rlkey=q63jtmue5qkp56h7kpspmk0qe&dl=0> and will be uploaded to Zenodo upon acceptance of the paper. All figures were made using Matplotlib <https://matplotlib.org/>. The format of the files and their contents are described in a document available on Zenodo, including an example Python script.

Appendix A Specification of the Empirical Wave Model

The empirical wave model contains statistical properties of the root-mean-square wave amplitude of lower band chorus waves. The dataset is derived from Van Allen Probes A and B measurements between January 2013 and July 2019. As detailed in Shen et al. (2019), whistler activity was selected outside the plasmopause using the electron cyclotron harmonic (ECH) wave power. The wave amplitude is parameterized by L -shell, MLT, magnetic latitude ($|\lambda_{MLAT}|$), and SML*. We include only waves observed near the equator with $|\lambda_{MLAT}| < 10^\circ$. The grid of the empirical wave model extends in L -shell from $L = 2$ to 6 with 0.2 L resolution. The model has 1 hour resolution in MLT and six geomagnetic activity bins. The geomagnetic activity bins are defined as $SML^* > -100$ nT, -500 nT $< SML^* < -100$ nT, -750 nT $< SML^* < -500$ nT, -1000 nT $< SML^* < -750$ nT, $SML^* < -1000$ nT. L -shells were determined using the TS05 magnetic field model (Shen et al., 2019). Bins with sampling times less than three minutes, corresponding to 180 samples, were not included. This was done to ensure the statistical significance of the model. The wave spectrum is assumed to be Gaussian, with a peak at $0.3 f_{ce}$ and a lower and upper cutoff between $\omega_{LC} = 0.05 f_{ce}$ and $\omega_{UC} = 0.55 f_{ce}$, respectively.

Before ingesting the wave model into the test particle simulation, the wave amplitudes are interpolated onto a new grid with double the resolution in each dimension in L and MLT. Waves are routinely observed at L -shells larger than the apogee of the Van Allen Probes (Meredith et al., 2020). To avoid the large discontinuity in wave amplitude at geosynchronous orbit due to lack of data, we attenuate the wave amplitude in each MLT bin out to $L = 8$. This is done using a Gaussian profile that peaks at $L = 6$. The empirical model is smoothed with a 2D Gaussian filter to remove any artifacts. Wave amplitudes were excluded outside of $L=8$ as the injected populations from the plasma sheet are not included in this study and magnetopause losses quickly remove the electrons at larger L -shells.

Higher order harmonics become dominant for ≥ 1 MeV electrons as they resonate with obliquely propagating waves (Shprits et al., 2006; Shprits & Ni, 2009). For a given energy above ~ 1 MeV and a fixed f_{pe}/f_{ce} ratio, resonance with oblique waves extends scattering and energization rates to lower equatorial pitch angle. This enables more MeV electrons to resonate at a single location and, consequently, causes a single electron to be in resonance at a larger range of magnetic latitudes. Broadening the magnetic latitudes of the wave region, while retaining the parallel propagating wave assumption, has a qualitatively similar affect. The increased magnetic field at higher magnetic latitudes

shifts the resonating electrons to higher energies. In addition, the increased latitudinal range permits MeV particles with lower equatorial pitch angles to resonant near their bounce point.

As described in Section 2.4, we assume the chorus waves propagate parallel to the magnetic field. The Van Allen Probes is able to measure the wave environment between $|\lambda_{MLAT}| = 20^\circ$. As a proxy for resonance with obliquely propagating waves, we increase the latitudinal range of the waves to 45° . We define the latitudinal profile as a flat-top Gaussian distribution

$$f(\lambda_{MLAT}) = B_{W,eq} \exp \left[\left(\frac{\lambda_{MLAT}^2}{2\sigma} \right)^P \right] \quad (A1)$$

where $B_{W,eq}$ is the equatorial wave amplitude, $\sigma = 0.4$, and $P = 2.5$. The latitudinal profile in equation A1 was applied in all MLT sectors. A simple comparison of the bounce averaged diffusion coefficients calculated using this method to the full calculation with oblique waves (J. M. Albert, 2005, 2007, 2008; J. Albert, 2018) within the 20° is provided in the supplemental material. Both the wave amplitude profile in magnetic latitude and the distribution of the latitudinal extent of the waves with respect to MLT can be easily adjusted to provide better agreement with observations or statistical distributions.

Appendix B Stochastic Modeling of Wave-Particle Interactions

Electrons resonate with whistler mode waves when the Doppler shifted wave frequency is a harmonic of the relativistic gyrofrequency. This is determined by the resonance condition:

$$\omega - kv_{\parallel} = \frac{n\Omega_e}{\gamma}, \quad n = 0, \pm 1, \pm 2, \dots \quad (B1)$$

where ω is the wave frequency, k is the wave number in the direction of propagation, v_{\parallel} is the parallel velocity of the particle, γ is the Lorentz factor, and n is an integer denoting the cyclotron harmonic. Ω_e is the nonrelativistic electron gyrofrequency defined by $|\Omega_e| = e|\mathbf{B}|/(m_e c)$, where \mathbf{B} is the magnetic field vector, m_e is the electron mass, and c is the speed of light. The resonant frequencies are obtained by simultaneously solving the resonance condition with the dispersion relation of the wave. For R mode whistler waves this is given by

$$\left(\frac{ck}{\omega} \right)^2 = 1 - \left(\frac{\omega_{pe}}{\Omega_e} \right)^2 \frac{1 + \epsilon}{(\omega/|\Omega_e| - 1)(\omega/|\Omega_e| + \epsilon)} \quad (B2)$$

where $\omega_{pe} = \sqrt{4\pi N_0 e^2 / m_e}$ is the plasma frequency, N_0 is the plasma density, and e is the electron charge. Finally, $\epsilon = m_e/m_p$ is the electron to proton mass ratio.

Many cyclotron harmonics contribute to electron resonance and scattering when waves propagate obliquely to the magnetic field (J. M. Albert & Young, 2005). Numerical codes that calculate diffusion rates for oblique waves often include resonance with ± 5 cyclotron harmonics (Horne et al., 2003; J. M. Albert & Young, 2005). While these codes are efficient, computation of diffusion rates including an angular spread in wave normal angle can still be computationally expensive. This is especially true when trying to integrate the calculation within a test particle approach. Test particles in our simulation undergo on the order of $\sim 10^8$ resonant interactions over the course of the storm main phase. Several million test particles are also needed to fully resolve phase space.

Lower band chorus waves tend to be quasi field-aligned, with their wave normal distribution peaking at 0° and are often approximated using an angular distribution of 30° (Horne et al., 2003). In addition, for 100 keV to a few MeV electrons, the bounce-averaged diffusion coefficients are dominated by the resonant harmonic associated with parallel propagating waves (Shprits et al., 2006). We, therefore, do not include the wave

normal distribution and assume waves propagate parallel to the magnetic field. The parallel propagation assumption significantly reduces the complexity of the computation, as electrons resonate with the first-order harmonic only (Summers et al., 1998). This enables us to quickly and efficiently determine the resonant wave frequency for each resonant wave-particle interaction. As discussed in Summers (2005), solution of equations (B1) and (B2) for parallel propagating waves yields up to potentially three resonant roots. We further assume that lower band chorus waves only propagate away from the equator. This assumption results in a single resonant frequency for each wave-particle interaction.

We solve the Fokker-Plank diffusion equation using a time-forward stochastic differential equation (SDE) to compute pitch angle scattering and momentum diffusion from resonant wave-particle interactions. Derived by Tao et al. (2008), the SDE is formulated using the Itô method and is defined as:

$$\begin{aligned}\Delta\alpha &= a_\alpha\Delta t + b_{\alpha\alpha}\sqrt{2\Delta t}\eta_\alpha \\ \Delta p &= a_p\Delta t + b_{p\alpha}\sqrt{2\Delta t}\eta_\alpha + b_{pp}\sqrt{2\Delta t}\eta_p\end{aligned}\tag{B3}$$

where

$$\begin{aligned}a_\alpha &= \frac{1}{Gp}\partial_\alpha\left(\frac{GD_{\alpha\alpha}}{p}\right) + \frac{1}{G}\partial_p\left(\frac{GD_{\alpha p}}{p}\right) \\ a_p &= \frac{1}{Gp}\partial_\alpha(GD_{\alpha p}) + \frac{1}{G}\partial_p(GD_{pp})\end{aligned}\tag{B4}$$

and $G = p^2 \sin \alpha$. The second term, and third for Δp , on the right-hand side of equations (B4) describe a Wiener process. η_α, η_p are separate random numbers generated from a normal distribution with a mean of zero and a variance of 1 and Δt represents the time the particle is in resonance with the wave. For real $D_{\alpha p} = D_{p\alpha}$, the diffusion matrix, \mathbf{b} , is overdetermined. Following Tao et al. (2008), we set $b_{\alpha p} = 0$. The diffusion matrix reduces to:

$$\begin{aligned}b_{\alpha\alpha} &= \sqrt{D_{\alpha\alpha}}/p, & b_{\alpha p} &= 0 \\ b_{p\alpha} &= D_{p\alpha}/\sqrt{D_{\alpha\alpha}}, & b_{pp} &= \sqrt{D_{pp} - D_{p\alpha}^2/D_{\alpha\alpha}}.\end{aligned}\tag{B5}$$

The local quasi-linear diffusion rates used here are defined such that $D_{\alpha\alpha}/p^2, D_{\alpha p}/p^2$, and D_{pp}/p^2 are in units of s^{-1} . This corresponds to the notation of Lyons (1974a, 1974b). Summers (2005) derived analytical expressions for the local $D_{\alpha\alpha}, D_{\alpha p}$ and D_{pp} . The derivation uses the exact cold plasma dispersion relationship and the resonance condition for field-aligned electromagnetic waves in a hydrogen plasma. Following Summers (2005), $D_{\alpha\alpha}, D_{\alpha p}$ and D_{pp} are defined as:

$$\begin{aligned}\frac{D_{\alpha\alpha}}{p^2} &= \frac{\pi}{4} \frac{\Omega_e^2}{W_0} \frac{1}{\gamma^2} \left(1 - \frac{\omega_j \cos \alpha}{k_j v}\right)^2 \frac{W(k_j)}{|v \cos \alpha - d\omega_j/dk_j|} \\ \frac{D_{\alpha p}}{p^2} &= -\frac{\pi}{4} \frac{\Omega_e^2}{W_0} \frac{\sin \alpha}{\beta \gamma^2} \left(1 - \frac{\omega_j \cos \alpha}{k_j v}\right) \left(\frac{\omega_j}{k_j}\right) \frac{W(k_j)}{|v \cos \alpha - d\omega_j/dk_j|} \\ \frac{D_{pp}}{p^2} &= -\frac{\pi}{4} \frac{\Omega_e^2}{W_0} \frac{\sin^2 \alpha}{\beta^2 \gamma^2} \left(\frac{\omega_j}{k_j}\right)^2 \frac{W(k_j)}{|v \cos \alpha - d\omega_j/dk_j|}\end{aligned}\tag{B6}$$

where α is the pitch angle, $W_0 = B_0^2/8\pi$ is the magnetic energy density of the background magnetic, ω_j and k_j are the resonant frequency and wave number that satisfy equation (B1) and (B2), and $\beta = v/c$, $d\omega_j/dk_j$ is obtained from equation (B1), and $W(k_j)$ is the wave spectral density. The diffusion coefficients differ from Summers (2005) by a factor of 2, as noted in J. M. Albert (2007). In addition to being faster to evaluate, the closed form expressions enable the model to solve for diffusion coefficients for each resonant interaction. The background magnetic field, density, and wave amplitude at each

electron's location are taken directly from either the global magnetosphere or empirical wave model. This removes the need to pre-compute or bounce-average the diffusion coefficients based on empirical density or magnetic field reconstructions. The analytical expressions also permits the local diffusion coefficients to vary throughout the storm as a function of time and 3D location. The advantage to this approach is the temporal variations of $D_{\alpha\alpha}$, $D_{\alpha p}$ and D_{pp} are physically consistent with the plasma conditions through which the test particle trajectories are being integrated.

The SDE is evaluated concurrently with the test particle integrator. The average state of the test particle over the time step is used in the wave-particle interaction to reduce any error introduced in operator splitting. The particle only experiences a resonant interaction if lower band chorus waves are present at the particle's location and if the resonant frequency resides between the lower and upper cutoff set for the spectrum. The location of the last equatorial crossing is used to determine the particle's L -shell. This assumes that the bounce timescale of the particle is much less than the drift motion and avoids the need to perform field line tracing for each individual interaction. To determine the corresponding wave amplitude from the empirical wave model, we compute dL_{pp} of the particle using the plasmapause location in the global magnetosphere model. The plasmapause location is calculated in the equatorial plane as a function of MLT, discretized into 5° bins. For each MLT bin, we define the plasmapause location where the plasma density first decreases to 100 cm^{-3} , as in Ripoll et al. (2022).

If present, the wave amplitude in the empirical wave model at the particle's dL_{pp} and MLT is retrieved. The wave amplitude is scaled according to the particle's magnetic latitude using equation A1. The magnetic field and density at the particle's location is obtained from the MAGE model. ω_j and k_j are calculated from the resonance condition and dispersion relation using the energy and pitch angle of the particle along with the background plasma conditions. $D_{\alpha\alpha}$, $D_{\alpha p}$, D_{pp} and their derivatives, are then computed and used within the SDE to determine the pitch angle scattering, $\Delta\alpha$, and momentum diffusion, Δp , of the particle. $\Delta\alpha$ and Δp are used to update the electron's momentum and energy according to $p_{new} = p_{initial} + \Delta p$, $\alpha_{new} = \alpha_{initial} + \Delta\alpha$, respectively. Δt in equation (B4) is initially set to the time step of the particle. To reduce error in the calculation, each resonant interaction is limited to not exceed $\Delta\alpha = 0.5^\circ$ or $\Delta p = 0.05 p_{initial}$. Δt is updated to ensure this criteria is met. The SDE is advances iteratively until the cumulative resonance time matches the original time step. The SDE is advanced every time step that the particle remains in resonance with waves, updating the particle energy, pitch angle, wave amplitude, and background magnetic field and density accordingly.

Appendix C Calculation of Bounce-Averaged Diffusion Coefficients

Bounce averaging is performed following a similar approach to Lyons et al. (1972); Shprits et al. (2006); Summers et al. (2007a). The local diffusion coefficients, $D_{\alpha\alpha}$ and $D_{\alpha p}$ are multiplied by $\left(\frac{\partial\alpha_{eq}}{\partial\alpha}\right)^2$, $\frac{\partial\alpha_{eq}}{\partial\alpha}$, respectively, to convert them to the equivalent equatorial coefficients, where

$$\frac{\partial\alpha_{eq}}{\partial\alpha} = \frac{\tan\alpha_{eq}}{\tan\alpha}. \quad (\text{C1})$$

The bounce-averaged values of the diffusion coefficients (B6) therefore become

$$\begin{aligned}\langle D_{\alpha\alpha} \rangle &= \frac{1}{\tau_b} \int_0^{\tau_b} D_{\alpha\alpha}(K, \alpha, B, \rho, B_w) \left(\frac{\partial \alpha_{eq}}{\partial \alpha} \right)^2 dt \\ \langle D_{\alpha p} \rangle &= \frac{1}{\tau_b} \int_0^{\tau_b} D_{\alpha p}(K, \alpha, B, \rho, B_w) \left(\frac{\partial \alpha_{eq}}{\partial \alpha} \right) dt \\ \langle D_{pp} \rangle &= \frac{1}{\tau_b} \int_0^{\tau_b} D_{pp}(K, \alpha, B, \rho, B_w) dt\end{aligned}\tag{C2}$$

where τ_B is the bounce-period of the particle and is defined as

$$\tau_b = 2 \int_{-S_{m1}}^{S_{m2}} \frac{ds}{v_{\parallel}} = \frac{2}{v} \int_{-S_{m1}}^{S_{m2}} \frac{1}{\sqrt{1 - \frac{B}{B_{eq}} \sin^2 \alpha_{eq}}} ds\tag{C3}$$

This converts the integral of the bounce period along the magnetic field line from one mirror point in the southern hemisphere, $-S_{m1}$, to the other mirror point in the northern hemisphere, S_{m2}

Similarly, we recast the integrals of the bounce averaged diffusion coefficients to be along the magnetic field line, as done in equation C3. We do not assume that the magnetic field is a dipole, rather we perform field line tracing in the MAGE model to extract the storm-time magnetic fields and density profile. Combining equations C1-C3, we obtain the new expressions

$$\begin{aligned}\langle D_{\alpha\alpha} \rangle &= \frac{1}{T(\alpha_{eq})} \int_{-S_{m1}}^{S_{m2}} D_{\alpha\alpha} \frac{\tan^2 \alpha_{eq} \cos \alpha(s)}{\sin^2 \alpha(s)} ds \\ \langle D_{\alpha p} \rangle &= \frac{1}{T(\alpha_{eq})} \int_{-S_{m1}}^{S_{m2}} D_{\alpha p} \frac{\tan \alpha_{eq}}{\sin \alpha(s)} ds \\ \langle D_{pp} \rangle &= \frac{1}{T(\alpha_{eq})} \int_{-S_{m1}}^{S_{m2}} D_{pp} \frac{1}{\cos \alpha(s)} ds\end{aligned}\tag{C4}$$

where $\alpha(s)$ is a function of α_{eq} and the magnetic field strength at a particular location along the field line, $B(s)$. $T(\alpha_{eq})$ is defined as $T(\alpha_{eq}) = \int_{-S_{m1}}^{S_{m2}} \frac{1}{\sqrt{1 - \frac{B}{B_{eq}} \sin^2 \alpha_{eq}}} ds$. To perform calculation of the bounce averaged diffusion coefficients for a given energy and α_{eq} , the resonant frequency and resulting local diffusion coefficient must be determined at each location along the discretized field line.

Acknowledgments

This work was supported by the NASA Early Career Investigator Program grant 80NSSC21K0464, Living With a Star grant 80NSSC17K0679, NASA O2R grant 80NSSC19K0241, the Van Allen Probes mission NNN06AA01C, as well as by the NASA DRIVE Science Center for Geospace Storms (CGS) under award 80NSSC20K0601. KS was also supported by 80NSSC20K1833. WL and XS acknowledge the NASA grant 80NSSC20K0698 and NSF grant AGS-1847818. We would like to acknowledge high-performance computing support from Cheyenne (doi:10.5065/D6RX99HX) provided by NCAR's Computational and Information Systems Laboratory, sponsored by the National Science Foundation.

References

Agapitov, O. V., Mourenas, D., Artemyev, A. V., Mozer, F. S., Hospodarsky, G., Bonnell, J., & Krasnoselskikh, V. (2018). Synthetic empirical chorus wave

- model from combined van allen probes and cluster statistics. *Journal of Geophysical Research: Space Physics*, 123(1), 297-314. Retrieved from <https://agupubs.onlinelibrary.wiley.com/doi/abs/10.1002/2017JA024843> doi: <https://doi.org/10.1002/2017JA024843>
- Albert, J. (2018). Diagonalization of diffusion equations in two and three dimensions. *Journal of Atmospheric and Solar-Terrestrial Physics*, 177, 202-207. Retrieved from <https://www.sciencedirect.com/science/article/pii/S1364682617302663> (Dynamics of the Sun-Earth System: Recent Observations and Predictions) doi: <https://doi.org/10.1016/j.jastp.2017.08.008>
- Albert, J. M. (2005). Evaluation of quasi-linear diffusion coefficients for whistler mode waves in a plasma with arbitrary density ratio. *Journal of Geophysical Research: Space Physics*, 110(A3). Retrieved from <https://agupubs.onlinelibrary.wiley.com/doi/abs/10.1029/2004JA010844> doi: <https://doi.org/10.1029/2004JA010844>
- Albert, J. M. (2007). Simple approximations of quasi-linear diffusion coefficients. *Journal of Geophysical Research: Space Physics*, 112(A12). Retrieved from <https://agupubs.onlinelibrary.wiley.com/doi/abs/10.1029/2007JA012551> doi: <https://doi.org/10.1029/2007JA012551>
- Albert, J. M. (2008). Efficient approximations of quasi-linear diffusion coefficients in the radiation belts. *Journal of Geophysical Research: Space Physics*, 113(A6). Retrieved from <https://agupubs.onlinelibrary.wiley.com/doi/abs/10.1029/2007JA012936> doi: <https://doi.org/10.1029/2007JA012936>
- Albert, J. M., & Young, S. L. (2005). Multidimensional quasi-linear diffusion of radiation belt electrons. *Geophysical Research Letters*, 32(14). Retrieved from <https://agupubs.onlinelibrary.wiley.com/doi/abs/10.1029/2005GL023191> doi: <https://doi.org/10.1029/2005GL023191>
- Allison, H. J., Shprits, Y. Y., Zhelavskaya, I. S., Wang, D., & Smirnov, A. G. (2021). Gyroresonant wave-particle interactions with chorus waves during extreme depletions of plasma density in the van allen radiation belts. *Science Advances*, 7(5), eabc0380. Retrieved from <https://www.science.org/doi/abs/10.1126/sciadv.abc0380> doi: [10.1126/sciadv.abc0380](https://doi.org/10.1126/sciadv.abc0380)
- Angelopoulos, V., Kennel, C. F., Coroniti, F. V., Pellat, R., Kivelson, M. G., Walker, R. J., ... Gosling, J. T. (1994). Statistical characteristics of bursty bulk flow events. *Journal of Geophysical Research: Space Physics*, 99(A11), 21257-21280. doi: [10.1029/94ja01263](https://doi.org/10.1029/94ja01263)
- Baker, D. N., Jaynes, A. N., Li, X., Henderson, M. G., Kanekal, S. G., Reeves, G. D., ... Shprits, Y. Y. (2014, March). Gradual diffusion and punctuated phase space density enhancements of highly relativistic electrons: Van Allen Probes observations. *Geophysical Research Letters*, 41(5), 1351-1358. doi: [10.1002/2013GL058942](https://doi.org/10.1002/2013GL058942)
- Baumjohann, W., Paschmann, G., & Lühr, H. (1990). Characteristics of high-speed ion flows in the plasma sheet. *Journal of Geophysical Research: Space Physics* (1978-2012), 95(A4), 3801-3809. doi: [10.1029/ja095ia04p03801](https://doi.org/10.1029/ja095ia04p03801)
- Blake, J. B., Carranza, P. A., Claudepierre, S. G., Clemmons, J. H., Crain, W. R., Dotan, Y., ... Zakrzewski, M. P. (2013, November). The Magnetic Electron Ion Spectrometer (MagEIS) Instruments Aboard the Radiation Belt Storm Probes (RBSP) Spacecraft. *Space Science Reviews*, 179(1-4), 383-421. doi: [10.1007/s11214-013-9991-8](https://doi.org/10.1007/s11214-013-9991-8)
- Borovsky, J. E., & Denton, M. H. (2006). Effect of plasmaspheric drainage plumes on solar-wind/magnetosphere coupling. *Geophysical Research Letters*, 33(20). Retrieved from <https://agupubs.onlinelibrary.wiley.com/doi/abs/10.1029/2006GL026519> doi: <https://doi.org/10.1029/2006GL026519>
- Boyd, A. J., Reeves, G. D., Spence, H. E., Funsten, H. O., Larsen, B. A., Skoug, R. M., ... Jaynes, A. N. (2019). Rbsp-ect combined spin-averaged electron flux data product. *Journal of Geophysical Research: Space Physics*,

- 124(11), 9124-9136. Retrieved from <https://agupubs.onlinelibrary.wiley.com/doi/abs/10.1029/2019JA026733> doi: <https://doi.org/10.1029/2019JA026733>
- Chan, A. A., Elkington, S. R., Longley, W. J., Aldhura, S. A., Alam, S. S., Albert, J. M., ... Li, W. (2023). Simulation of radiation belt wave-particle interactions in an mhd-particle framework. *Frontiers in Astronomy and Space Sciences*, 10. Retrieved from <https://www.frontiersin.org/articles/10.3389/fspas.2023.1239160> doi: 10.3389/fspas.2023.1239160
- Claudepierre, S. G., Toffoletto, F. R., & Wiltberger, M. (2016). Global mhd modeling of resonant ulf waves: Simulations with and without a plasmasphere. *Journal of Geophysical Research: Space Physics*, 121(1), 227–244. doi: 10.1002/2015ja022048
- Darrouzet, F., Gallagher, D. L., André, N., Carpenter, D. L., Dandouras, I., Décréau, P. M. E., ... et al. (2009). Plasmaspheric density structures and dynamics: Properties observed by the cluster and image missions. *Space Science Reviews*, 145(1–2), 55–106. doi: 10.1007/s11214-008-9438-9
- Delzanno, G. L., Borovsky, J. E., Henderson, M. G., Resendiz Lira, P. A., Roytershteyn, V., & Welling, D. T. (2021). The impact of cold electrons and cold ions in magnetospheric physics. *Journal of Atmospheric and Solar-Terrestrial Physics*, 220, 105599. Retrieved from <https://www.sciencedirect.com/science/article/pii/S1364682621000596> doi: <https://doi.org/10.1016/j.jastp.2021.105599>
- Denton, R. E., Wang, Y., Webb, P. A., Tengdin, P. M., Goldstein, J., Redfern, J. A., & Reinisch, B. W. (2012, March). Magnetospheric electron density long-term (>1 day) refilling rates inferred from passive radio emissions measured by IMAGE RPI during geomagnetically quiet times. *Journal of Geophysical Research (Space Physics)*, 117(A3), A03221. doi: 10.1029/2011JA017274
- Foster, J. C., & Burke, W. J. (2002). Saps: A new categorization for sub-auroral electric fields. *Eos, Transactions American Geophysical Union*, 83(36), 393–394. Retrieved from <https://agupubs.onlinelibrary.wiley.com/doi/abs/10.1029/2002EO000289> doi: <https://doi.org/10.1029/2002EO000289>
- Foster, J. C., Wygant, J. R., Hudson, M. K., Boyd, A. J., Baker, D. N., Erickson, P. J., & Spence, H. E. (2015). Shock-induced prompt relativistic electron acceleration in the inner magnetosphere. *Journal of Geophysical Research: Space Physics*, 120(3), 1661–1674. Retrieved from <https://agupubs.onlinelibrary.wiley.com/doi/abs/10.1002/2014JA020642> doi: <https://doi.org/10.1002/2014JA020642>
- Gabriel, C., Angelopoulos, V., Harris, C., Artemyev, A., Kepko, L., & Runov, A. (2017). Extensive electron transport and energization via multiple, localized dipolarizing flux bundles. *Journal of Geophysical Research: Space Physics*, 122(5), 5059–5076. Retrieved from <https://agupubs.onlinelibrary.wiley.com/doi/abs/10.1002/2017JA023981> doi: 10.1002/2017JA023981
- Gallagher, D. L., Craven, P. D., & Comfort, R. H. (2000). Global core plasma model. *Journal of Geophysical Research: Space Physics*, 105(A8), 18819–18833. Retrieved from <https://agupubs.onlinelibrary.wiley.com/doi/abs/10.1029/1999JA000241> doi: 10.1029/1999JA000241
- Gjerloev, J. W. (2012). The SuperMAG data processing technique. *Journal of Geophysical Research: Space Physics*, 117(A9). Retrieved 2022-08-30, from <https://onlinelibrary.wiley.com/doi/abs/10.1029/2012JA017683> (eprint: <https://onlinelibrary.wiley.com/doi/pdf/10.1029/2012JA017683>) doi: 10.1029/2012JA017683
- Goldstein, J., & Sandel, B. R. (2005). The global pattern of evolution of plasmaspheric drainage plumes. In *Inner magnetosphere interactions: New perspectives from imaging* (p. 1-22). American Geophysical Union (AGU). Retrieved from <https://agupubs.onlinelibrary.wiley.com/doi/abs/10.1029/159GM02>

- doi: <https://doi.org/10.1029/159GM02>
- Grebowsky, J. M. (1970). Model study of plasmopause motion. *Journal of Geophysical Research (1896-1977)*, 75(22), 4329-4333. Retrieved from <https://agupubs.onlinelibrary.wiley.com/doi/abs/10.1029/JA075i022p04329>
- doi: <https://doi.org/10.1029/JA075i022p04329>
- Horne, R. B., Glauert, S. A., & Thorne, R. M. (2003). Resonant diffusion of radiation belt electrons by whistler-mode chorus. *Geophysical Research Letters*, 30(9). Retrieved from <https://agupubs.onlinelibrary.wiley.com/doi/abs/10.1029/2003GL016963> doi: <https://doi.org/10.1029/2003GL016963>
- Hudson, M. K., Paral, J., Kress, B. T., Wiltberger, M., Baker, D. N., Foster, J. C., ... Wygant, J. R. (2015). Modeling cme-shock-driven storms in 2012–2013: Mhd test particle simulations. *Journal of Geophysical Research: Space Physics*, 120(2), 1168-1181. Retrieved from <https://agupubs.onlinelibrary.wiley.com/doi/abs/10.1002/2014JA020833> doi: <https://doi.org/10.1002/2014JA020833>
- Jaynes, A. N., Baker, D. N., Singer, H. J., Rodriguez, J. V., Loto'aniu, T. M., Ali, A. F., ... Reeves, G. D. (2015). Source and seed populations for relativistic electrons: Their roles in radiation belt changes. *Journal of Geophysical Research: Space Physics*, 120(9), 7240-7254. Retrieved from <https://agupubs.onlinelibrary.wiley.com/doi/abs/10.1002/2015JA021234> doi: <https://doi.org/10.1002/2015JA021234>
- Kennel, C. F., & Petschek, H. E. (1966). Limit on stably trapped particle fluxes. *Journal of Geophysical Research*, 71(1), 1–28. doi: 10.1029/jz071i001p00001
- Kim, H.-J., Kim, K.-C., Noh, S.-J., Lyons, L., Lee, D.-Y., & Choe, W. (2023). New perspective on phase space density analysis for outer radiation belt enhancements: The influence of mev electron injections. *Geophysical Research Letters*, 50(14), e2023GL104614. Retrieved from <https://agupubs.onlinelibrary.wiley.com/doi/abs/10.1029/2023GL104614> (e2023GL104614 2023GL104614) doi: <https://doi.org/10.1029/2023GL104614>
- Kress, B. T., Hudson, M. K., Ukhorskiy, A. Y., & Mueller, H.-R. (2012). Non-linear radial transport in the earth's radiation belts. In *Dynamics of the earth's radiation belts and inner magnetosphere* (p. 151-160). American Geophysical Union (AGU). Retrieved from <https://agupubs.onlinelibrary.wiley.com/doi/abs/10.1029/2012GM001333> doi: <https://doi.org/10.1029/2012GM001333>
- Li, W., Bortnik, J., Thorne, R. M., & Angelopoulos, V. (2011). Global distribution of wave amplitudes and wave normal angles of chorus waves using themis wave observations. *Journal of Geophysical Research: Space Physics*, 116(A12). Retrieved from <https://agupubs.onlinelibrary.wiley.com/doi/abs/10.1029/2011JA017035> doi: <https://doi.org/10.1029/2011JA017035>
- Li, W., & Hudson, M. (2019). Earth's Van Allen Radiation Belts: From Discovery to the Van Allen Probes Era. *Journal of Geophysical Research: Space Physics*, 124(11), 8319–8351. doi: 10.1029/2018ja025940
- Li, W., Ma, Q., Thorne, R. M., Bortnik, J., Kletzing, C. A., Kurth, W. S., ... Nishimura, Y. (2015). Statistical properties of plasmaspheric hiss derived from van allen probes data and their effects on radiation belt electron dynamics. *Journal of Geophysical Research: Space Physics*, 120(5), 3393-3405. Retrieved from <https://agupubs.onlinelibrary.wiley.com/doi/abs/10.1002/2015JA021048> doi: <https://doi.org/10.1002/2015JA021048>
- Li, W., Santolik, O., Bortnik, J., Thorne, R. M., Kletzing, C. A., Kurth, W. S., & Hospodarsky, G. B. (2016). New chorus wave properties near the equator from van allen probes wave observations. *Geophysical Research Letters*, 43(10), 4725-4735. Retrieved from <https://agupubs.onlinelibrary.wiley.com/doi/abs/10.1002/2016GL068780> doi: <https://doi.org/10.1002/2016GL068780>

- Li, W., Thorne, R. M., Ma, Q., Ni, B., Bortnik, J., Baker, D. N., ... Claude-
pierre, S. G. (2014). Radiation belt electron acceleration by chorus
waves during the 17 march 2013 storm. *Journal of Geophysical Re-
search: Space Physics*, 119(6), 4681-4693. Retrieved from [https://
agupubs.onlinelibrary.wiley.com/doi/abs/10.1002/2014JA019945](https://agupubs.onlinelibrary.wiley.com/doi/abs/10.1002/2014JA019945) doi:
<https://doi.org/10.1002/2014JA019945>
- Li, Z., Hudson, M., Kress, B., & Paral, J. (2015). Three-dimensional test par-
ticle simulation of the 17–18 march 2013 cme shock-driven storm. *Geo-
physical Research Letters*, 42(14), 5679-5685. Retrieved from [https://
agupubs.onlinelibrary.wiley.com/doi/abs/10.1002/2015GL064627](https://agupubs.onlinelibrary.wiley.com/doi/abs/10.1002/2015GL064627) doi:
<https://doi.org/10.1002/2015GL064627>
- Lin, D., Sorathia, K., Wang, W., Merkin, V., Bao, S., Pham, K., ... et al.
(2021). The role of diffuse electron precipitation in the formation of sub-
auroral polarization streams. *Earth and Space Science Open Archive*, 20.
Retrieved from <https://doi.org/10.1002/essoar.10508315.1> doi:
[10.1002/essoar.10508315.1](https://doi.org/10.1002/essoar.10508315.1)
- Longley, W. J., Chan, A. A., Jaynes, A. N., Elkington, S. R., Pettit, J. M., Ross,
J. P. J., ... Horne, R. B. (2022). Using meped observations to infer plasma
density and chorus intensity in the radiation belts. *Frontiers in Astronomy and
Space Sciences*, 9. Retrieved from [https://www.frontiersin.org/articles/
10.3389/fspas.2022.1063329](https://www.frontiersin.org/articles/10.3389/fspas.2022.1063329) doi: 10.3389/fspas.2022.1063329
- Lyons, L. R. (1974a). General relations for resonant particle diffusion in
pitch angle and energy. *Journal of Plasma Physics*, 12(1), 45–49. doi:
[10.1017/S0022377800024910](https://doi.org/10.1017/S0022377800024910)
- Lyons, L. R. (1974b). Pitch angle and energy diffusion coefficients from resonant in-
teractions with ion-cyclotron and whistler waves. *Journal of Plasma Physics*,
12(3), 417–432. doi: [10.1017/S002237780002537X](https://doi.org/10.1017/S002237780002537X)
- Lyons, L. R., Thorne, R. M., & Kennel, C. F. (1972, January). Pitch-angle diffusion
of radiation belt electrons within the plasmasphere. *Journal of Geophysical Re-
search*, 77(19), 3455. doi: [10.1029/JA077i019p03455](https://doi.org/10.1029/JA077i019p03455)
- Ma, Q., Li, W., Bortnik, J., Thorne, R. M., Chu, X., Ozeke, L. G., ... Claude-
pierre, S. G. (2018). Quantitative evaluation of radial diffusion and local
acceleration processes during gem challenge events. *Journal of Geophysi-
cal Research: Space Physics*, 123(3), 1938-1952. Retrieved from [https://
agupubs.onlinelibrary.wiley.com/doi/abs/10.1002/2017JA025114](https://agupubs.onlinelibrary.wiley.com/doi/abs/10.1002/2017JA025114) doi:
<https://doi.org/10.1002/2017JA025114>
- Malaspina, D. M., Jaynes, A. N., Boulé, C., Bortnik, J., Thaller, S. A., Ergun, R. E.,
... Wygant, J. R. (2016). The distribution of plasmaspheric hiss wave power
with respect to plasmopause location. *Geophysical Research Letters*, 43(15),
7878–7886. doi: [10.1002/2016gl069982](https://doi.org/10.1002/2016gl069982)
- Meredith, N. P., Cain, M., Horne, R. B., Thorne, R. M., Summers, D., & Anderson,
R. R. (2003). Evidence for chorus-driven electron acceleration to relativis-
tic energies from a survey of geomagnetically disturbed periods. *Journal of
Geophysical Research: Space Physics*, 108(A6). Retrieved from [https://
agupubs.onlinelibrary.wiley.com/doi/abs/10.1029/2002JA009764](https://agupubs.onlinelibrary.wiley.com/doi/abs/10.1029/2002JA009764) doi:
<https://doi.org/10.1029/2002JA009764>
- Meredith, N. P., Horne, R. B., Shen, X.-C., Li, W., & Bortnik, J. (2020). Global
model of whistler mode chorus in the near-equatorial region ($|\lambda_m| < 18^\circ$). *Geo-
physical Research Letters*, 47(11), e2020GL087311. Retrieved from [https://
agupubs.onlinelibrary.wiley.com/doi/abs/10.1029/2020GL087311](https://agupubs.onlinelibrary.wiley.com/doi/abs/10.1029/2020GL087311)
(e2020GL087311 10.1029/2020GL087311) doi: [https://doi.org/10.1029/
2020GL087311](https://doi.org/10.1029/2020GL087311)
- Meredith, N. P., Horne, R. B., Sicard-Piet, A., Boscher, D., Yearby, K. H., Li,
W., & Thorne, R. M. (2012). Global model of lower band and up-
per band chorus from multiple satellite observations. *Journal of Geo-*

- physical Research: *Space Physics*, 117(A10). Retrieved from <https://agupubs.onlinelibrary.wiley.com/doi/abs/10.1029/2012JA017978> doi: <https://doi.org/10.1029/2012JA017978>
- Merkin, V. G., & Lyon, J. G. (2010, Oct). Effects of the low-latitude ionospheric boundary condition on the global magnetosphere. *Journal of Geophysical Research (Space Physics)*, 115(A10), A10202. doi: 10.1029/2010JA015461
- Millan, R., & Thorne, R. (2007). Review of radiation belt relativistic electron losses. *Journal of Atmospheric and Solar-Terrestrial Physics*, 69(3), 362-377. Retrieved from <https://www.sciencedirect.com/science/article/pii/S1364682606002768> (Global Aspects of Magnetosphere-Ionosphere Coupling) doi: <https://doi.org/10.1016/j.jastp.2006.06.019>
- Newell, P. T., & Gjerloev, J. W. (2012). SuperMAG-based partial ring current indices. *Journal of Geophysical Research: Space Physics*, 117(A5). Retrieved 2022-08-30, from <https://onlinelibrary.wiley.com/doi/abs/10.1029/2012JA017586> (_eprint: <https://onlinelibrary.wiley.com/doi/pdf/10.1029/2012JA017586>) doi: 10.1029/2012JA017586
- Newell, P. T., & Gjerloev, J. W. (2014). Local geomagnetic indices and the prediction of auroral power. *Journal of Geophysical Research: Space Physics*, 119(12), 9790-9803. Retrieved 2022-08-30, from <https://onlinelibrary.wiley.com/doi/abs/10.1002/2014JA020524> (_eprint: <https://onlinelibrary.wiley.com/doi/pdf/10.1002/2014JA020524>) doi: 10.1002/2014JA020524
- Pembroke, A., Toffoletto, F., Sazykin, S., Wiltberger, M., Lyon, J., Merkin, V., & Schmitt, P. (2012). Initial results from a dynamic coupled magnetosphere-ionosphere-ring current model. *Journal of Geophysical Research: Space Physics*, 117(A2). Retrieved from <https://agupubs.onlinelibrary.wiley.com/doi/abs/10.1029/2011JA016979> doi: 10.1029/2011JA016979
- Pham, K. H., Zhang, B., Sorathia, K., Dang, T., Wang, W., Merkin, V., ... Lyon, J. (2022, February). Thermospheric Density Perturbations Produced by Traveling Atmospheric Disturbances During August 2005 Storm. *Journal of Geophysical Research (Space Physics)*, 127(2), e2021JA030071. doi: 10.1029/2021JA030071
- Reeves, G. D., McAdams, K. L., Friedel, R. H. W., & O'Brien, T. P. (2003). Acceleration and loss of relativistic electrons during geomagnetic storms. *Geophysical Research Letters*, 30(10). Retrieved from <https://agupubs.onlinelibrary.wiley.com/doi/abs/10.1029/2002GL016513> doi: <https://doi.org/10.1029/2002GL016513>
- Ripoll, J.-F., Claudepierre, S. G., Ukhorskiy, A. Y., Colpitts, C., Li, X., Fennell, J. F., & Crabtree, C. (2020). Particle dynamics in the earth's radiation belts: Review of current research and open questions. *Journal of Geophysical Research: Space Physics*, 125(5), e2019JA026735. Retrieved from <https://agupubs.onlinelibrary.wiley.com/doi/abs/10.1029/2019JA026735> (e2019JA026735 2019JA026735) doi: <https://doi.org/10.1029/2019JA026735>
- Ripoll, J.-F., Thaller, S. A., Hartley, D. P., Cunningham, G. S., Pierrard, V., Kurth, W. S., ... Wygant, J. R. (2022). Statistics and empirical models of the plasmasphere boundaries from the van allen probes for radiation belt physics. *Geophysical Research Letters*, 49(21), e2022GL101402. Retrieved from <https://agupubs.onlinelibrary.wiley.com/doi/abs/10.1029/2022GL101402> (e2022GL101402 2022GL101402) doi: <https://doi.org/10.1029/2022GL101402>
- Schulz, M. (1974). Particle lifetimes in strong diffusion. *Astrophysics and Space Science*, 31(1), 37-42. doi: 10.1007/bf00642599
- Sciola, A., Merkin, V. G., Sorathia, K. A., Gkioulidou, M., Bao, S., Toffoletto, F., ... Ukhorskiy, A. Y. (2023). The contribution of plasma sheet bubbles to stormtime ring current buildup and evolution of the energy composition. *Au-*

- thorea. doi: DOI:10.22541/essoar.168677230.00750251/v1
- Sheeley, B. W., Moldwin, M. B., Rassoul, H. K., & Anderson, R. R. (2001). An empirical plasmasphere and trough density model: Ceres observations. *Journal of Geophysical Research: Space Physics*, 106(A11), 25631-25641. Retrieved from <https://agupubs.onlinelibrary.wiley.com/doi/abs/10.1029/2000JA000286> doi: <https://doi.org/10.1029/2000JA000286>
- Shen, X.-C., Li, W., Ma, Q., Agapitov, O., & Nishimura, Y. (2019). Statistical analysis of transverse size of lower band chorus waves using simultaneous multisatellite observations. *Geophysical Research Letters*, 46(11), 5725-5734. Retrieved from <https://agupubs.onlinelibrary.wiley.com/doi/abs/10.1029/2019GL083118> doi: <https://doi.org/10.1029/2019GL083118>
- Shprits, Y. Y., Elkington, S. R., Meredith, N. P., & Subbotin, D. A. (2008). Review of modeling of losses and sources of relativistic electrons in the outer radiation belt i: Radial transport. *Journal of Atmospheric and Solar-Terrestrial Physics*, 70(14), 1679-1693. Retrieved from <https://www.sciencedirect.com/science/article/pii/S1364682608001648> (Dynamic Variability of Earth's Radiation Belts) doi: <https://doi.org/10.1016/j.jastp.2008.06.008>
- Shprits, Y. Y., & Ni, B. (2009). Dependence of the quasi-linear scattering rates on the wave normal distribution of chorus waves. *Journal of Geophysical Research: Space Physics*, 114(A11). Retrieved from <https://agupubs.onlinelibrary.wiley.com/doi/abs/10.1029/2009JA014223> doi: <https://doi.org/10.1029/2009JA014223>
- Shprits, Y. Y., Subbotin, D. A., Meredith, N. P., & Elkington, S. R. (2008). Review of modeling of losses and sources of relativistic electrons in the outer radiation belt ii: Local acceleration and loss. *Journal of Atmospheric and Solar-Terrestrial Physics*, 70(14), 1694-1713. Retrieved from <https://www.sciencedirect.com/science/article/pii/S1364682608001673> (Dynamic Variability of Earth's Radiation Belts) doi: <https://doi.org/10.1016/j.jastp.2008.06.014>
- Shprits, Y. Y., Thorne, R. M., Horne, R. B., & Summers, D. (2006). Bounce-averaged diffusion coefficients for field-aligned chorus waves. *Journal of Geophysical Research: Space Physics*, 111(A10). Retrieved from <https://agupubs.onlinelibrary.wiley.com/doi/abs/10.1029/2006JA011725> doi: <https://doi.org/10.1029/2006JA011725>
- Sorathia, K. A., Merkin, V. G., Panov, E. V., Zhang, B., Lyon, J. G., Garrettson, J., ... Wiltberger, M. (2020). Ballooning-interchange instability in the near-earth plasma sheet and auroral beads: Global magnetospheric modeling at the limit of the mhd approximation. *Geophysical Research Letters*, 47(14), e2020GL088227. Retrieved from <https://agupubs.onlinelibrary.wiley.com/doi/abs/10.1029/2020GL088227> (e2020GL088227 10.1029/2020GL088227) doi: 10.1029/2020GL088227
- Sorathia, K. A., Merkin, V. G., Ukhorskiy, A. Y., Allen, R. C., Nykyri, K., & Wing, S. (2019). Solar wind ion entry into the magnetosphere during northward imf. *Journal of Geophysical Research: Space Physics*, 124(7), 5461-5481. Retrieved from <https://agupubs.onlinelibrary.wiley.com/doi/abs/10.1029/2019JA026728> doi: <https://doi.org/10.1029/2019JA026728>
- Sorathia, K. A., Merkin, V. G., Ukhorskiy, A. Y., Mauk, B. H., & Sibeck, D. G. (2017). Energetic particle loss through the magnetopause: A combined global mhd and test-particle study. *Journal of Geophysical Research: Space Physics*, 122(9), 9329-9343. doi: 10.1002/2017ja024268
- Sorathia, K. A., Michael, A., Merkin, V., Ukhorskiy, A., Turner, D. L., Lyon, J., ... Toffoletto, F. (2021). The role of mesoscale plasma sheet dynamics in ring current formation. *Frontiers in Astronomy and Space Sciences*, 8. Retrieved from <https://www.frontiersin.org/articles/10.3389/fspas.2021.761875> doi: 10.3389/fspas.2021.761875

- Sorathia, K. A., Michael, A. T., Merkin, V. G., Ohtani, S., Keesee, A. M., Lin, D., ... Pulkkinen, A. (2023, submitted). Multiscale magnetosphere-ionosphere coupling during stormtime: A case study of the dawnside current wedge. *Journal of Geophysical Research: Space Physics*.
- Sorathia, K. A., Ukhorskiy, A. Y., Merkin, V. G., Fennell, J. F., & Claudepierre, S. G. (2018, Jul). Modeling the Depletion and Recovery of the Outer Radiation Belt During a Geomagnetic Storm: Combined MHD and Test Particle Simulations. *Journal of Geophysical Research (Space Physics)*, 123(7), 5590-5609. doi: 10.1029/2018JA025506
- Spence, H. E., Reeves, G. D., Baker, D. N., Blake, J. B., Bolton, M., Bourdarie, S., ... Thorne, R. M. (2013, November). Science Goals and Overview of the Radiation Belt Storm Probes (RBSP) Energetic Particle, Composition, and Thermal Plasma (ECT) Suite on NASA's Van Allen Probes Mission. *Space Science Reviews*, 179(1-4), 311-336. doi: 10.1007/s11214-013-0007-5
- Staples, F. A., Kellerman, A., Murphy, K. R., Rae, I. J., Sandhu, J. K., & Forsyth, C. (2022). Resolving magnetopause shadowing using multimission measurements of phase space density. *Journal of Geophysical Research: Space Physics*, 127(2), e2021JA029298. Retrieved from <https://agupubs.onlinelibrary.wiley.com/doi/abs/10.1029/2021JA029298> (e2021JA029298 2021JA029298) doi: <https://doi.org/10.1029/2021JA029298>
- Summers, D. (2005, Aug). Quasi-linear diffusion coefficients for field-aligned electromagnetic waves with applications to the magnetosphere. *Journal of Geophysical Research (Space Physics)*, 110(A8), A08213. doi: 10.1029/2005JA011159
- Summers, D., Ni, B., & Meredith, N. P. (2007a). Timescales for radiation belt electron acceleration and loss due to resonant wave-particle interactions: 1. theory. *Journal of Geophysical Research: Space Physics (1978-2012)*, 112(A4), n/a-n/a. doi: 10.1029/2006ja011801
- Summers, D., Ni, B., & Meredith, N. P. (2007b). Timescales for radiation belt electron acceleration and loss due to resonant wave-particle interactions: 2. evaluation for vlf chorus, elf hiss, and electromagnetic ion cyclotron waves. *Journal of Geophysical Research: Space Physics*, 112(A4). Retrieved from <https://agupubs.onlinelibrary.wiley.com/doi/abs/10.1029/2006JA011993> doi: <https://doi.org/10.1029/2006JA011993>
- Summers, D., Thorne, R. M., & Xiao, F. (1998). Relativistic theory of wave-particle resonant diffusion with application to electron acceleration in the magnetosphere. *Journal of Geophysical Research: Space Physics*, 103(A9), 20487-20500. Retrieved from <https://agupubs.onlinelibrary.wiley.com/doi/abs/10.1029/98JA01740> doi: 10.1029/98JA01740
- Tao, X., Chan, A. A., Albert, J. M., & Miller, J. A. (2008). Stochastic modeling of multidimensional diffusion in the radiation belts. *Journal of Geophysical Research: Space Physics*, 113(A7). Retrieved from <https://agupubs.onlinelibrary.wiley.com/doi/abs/10.1029/2007JA012985> doi: <https://doi.org/10.1029/2007JA012985>
- Thorne, R. M. (2010). Radiation belt dynamics: The importance of wave-particle interactions. *Geophysical Research Letters*, 37(22). Retrieved from <https://agupubs.onlinelibrary.wiley.com/doi/abs/10.1029/2010GL044990> doi: <https://doi.org/10.1029/2010GL044990>
- Toffoletto, F., Sazykin, S., Spiro, R., & Wolf, R. (2003). Inner magnetospheric modeling with the Rice Convection Model. *Space Science Reviews*, 107(1-2), 175-196. doi: 10.1023/a:1025532008047
- Turner, D. L., Cohen, I. J., Michael, A., Sorathia, K., Merkin, S., Mauk, B. H., ... Reeves, G. D. (2021). Can earth's magnetotail plasma sheet produce a source of relativistic electrons for the radiation belts? *Geophysical Research Letters*, 48(21), e2021GL095495. Retrieved from <https://agupubs.onlinelibrary.wiley.com/doi/abs/10.1029/2021GL095495>

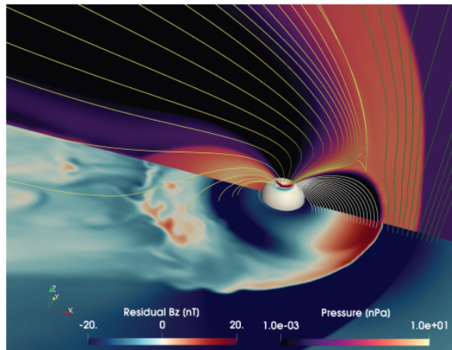
- (e2021GL095495 2021GL095495) doi: <https://doi.org/10.1029/2021GL095495>
- Turner, D. L., Fennell, J. F., Blake, J. B., Claudepierre, S. G., Clemmons, J. H., Jaynes, A. N., ... Reeves, G. D. (2017). Multipoint observations of energetic particle injections and substorm activity during a conjunction between magnetospheric multiscale (mms) and van allen probes. *Journal of Geophysical Research: Space Physics*, 122(11), 11,481-11,504. doi: 10.1002/2017ja024554
- Ukhorskiy, A. Y., Anderson, B. J., Brandt, P. C., & Tsyganenko, N. A. (2006). Storm time evolution of the outer radiation belt: Transport and losses. *Journal of Geophysical Research: Space Physics*, 111(A11). Retrieved from <https://agupubs.onlinelibrary.wiley.com/doi/abs/10.1029/2006JA011690> doi: <https://doi.org/10.1029/2006JA011690>
- Ukhorskiy, A. Y., & Sitnov, M. I. (2013, November). Dynamics of Radiation Belt Particles. *Space Science Reviews*, 179(1-4), 545-578. doi: 10.1007/s11214-012-9938-5
- Ukhorskiy, A. Y., Sitnov, M. I., Millan, R. M., & Kress, B. T. (2011). The role of drift orbit bifurcations in energization and loss of electrons in the outer radiation belt. *Journal of Geophysical Research: Space Physics*, 116(A9). Retrieved from <https://agupubs.onlinelibrary.wiley.com/doi/abs/10.1029/2011JA016623> doi: <https://doi.org/10.1029/2011JA016623>
- Ukhorskiy, A. Y., Sitnov, M. I., Millan, R. M., Kress, B. T., Fennell, J. F., Claudepierre, S. G., & Barnes, R. J. (2015). Global storm time depletion of the outer electron belt. *Journal of Geophysical Research: Space Physics*, 120(4), 2543-2556. Retrieved from <https://agupubs.onlinelibrary.wiley.com/doi/abs/10.1002/2014JA020645> doi: <https://doi.org/10.1002/2014JA020645>
- Ukhorskiy, A. Y., Sorathia, K. A., Merkin, V. G., Sitnov, M. I., Mitchell, D. G., & Gkioulidou, M. (2018). Ion trapping and acceleration at dipolarization fronts: High-resolution mhd and test-particle simulations. *Journal of Geophysical Research: Space Physics*, 123(7), 5580-5589. Retrieved from <https://agupubs.onlinelibrary.wiley.com/doi/abs/10.1029/2018JA025370> doi: <https://doi.org/10.1029/2018JA025370>
- Wang, D., Shprits, Y. Y., Zhelavskaya, I. S., Agapitov, O. V., Drozdov, A. Y., & Aseev, N. A. (2019). Analytical chorus wave model derived from van allen probe observations. *Journal of Geophysical Research: Space Physics*, 124(2), 1063-1084. Retrieved from <https://agupubs.onlinelibrary.wiley.com/doi/abs/10.1029/2018JA026183> doi: <https://doi.org/10.1029/2018JA026183>
- Wiltberger, M., Merkin, V., Zhang, B., Toffoletto, F., Oppenheim, M., Wang, W., ... Stephens, G. K. (2017). Effects of electrojet turbulence on a magnetosphere-ionosphere simulation of a geomagnetic storm. *Journal of Geophysical Research: Space Physics*, 122(5), 5008-5027. doi: 10.1002/2016ja023700
- Zhang, B., Sorathia, K. A., Lyon, J. G., Merkin, V. G., Garretson, J. S., & Wiltberger, M. (2019, sep). GAMERA: A three-dimensional finite-volume MHD solver for non-orthogonal curvilinear geometries. *The Astrophysical Journal Supplement Series*, 244(1), 20. Retrieved from <https://doi.org/10.3847/1538-4365/ab3a4c> doi: 10.3847/1538-4365/ab3a4c
- Zhao, H., Baker, D. N., Li, X., Jaynes, A. N., & Kanekal, S. G. (2019). The effects of geomagnetic storms and solar wind conditions on the ultrarelativistic electron flux enhancements. *Journal of Geophysical Research: Space Physics*, 124(3), 1948-1965. Retrieved from <https://agupubs.onlinelibrary.wiley.com/doi/abs/10.1029/2018JA026257> doi: <https://doi.org/10.1029/2018JA026257>
- Zheng, L., Chan, A. A., Albert, J. M., Elkington, S. R., Koller, J., Horne, R. B., ... Meredith, N. P. (2014). Three-dimensional stochastic modeling of radiation belts in adiabatic invariant coordinates. *Journal of Geophysi-*

1272 *cal Research: Space Physics*, 119(9), 7615-7635. Retrieved from [https://](https://agupubs.onlinelibrary.wiley.com/doi/abs/10.1002/2014JA020127)
1273 agupubs.onlinelibrary.wiley.com/doi/abs/10.1002/2014JA020127 doi:
1274 <https://doi.org/10.1002/2014JA020127>
1275 Zheng, L., Chen, L., Chan, A. A., Wang, P., Xia, Z., & Liu, X. (2021). Uber v1.0:
1276 a universal kinetic equation solver for radiation belts. *Geoscientific Model De-*
1277 *velopment*, 14(9), 5825–5842. Retrieved from [https://gmd.copernicus.org/](https://gmd.copernicus.org/articles/14/5825/2021/)
1278 [articles/14/5825/2021/](https://gmd.copernicus.org/articles/14/5825/2021/) doi: 10.5194/gmd-14-5825-2021

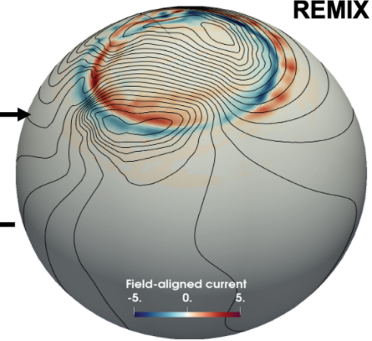
Figure 1.

Multiscale Atmosphere Geospace Environment Model

GAMERA



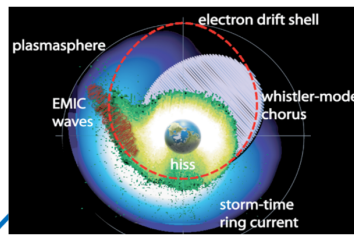
REMIX



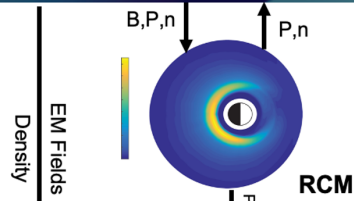
Currents and plasma moments

High Latitude Electric Field

Data Driven Wave Model



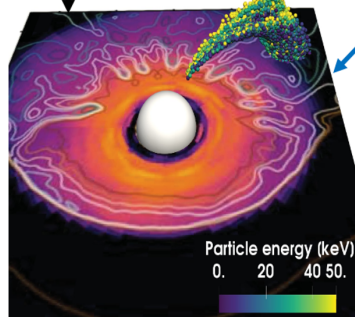
Hiss, chorus, EMIC



EM Fields

Density

Wave Information



CHIMP



MAGE
Multiscale Atmosphere-Geospace Environment

Figure 2.

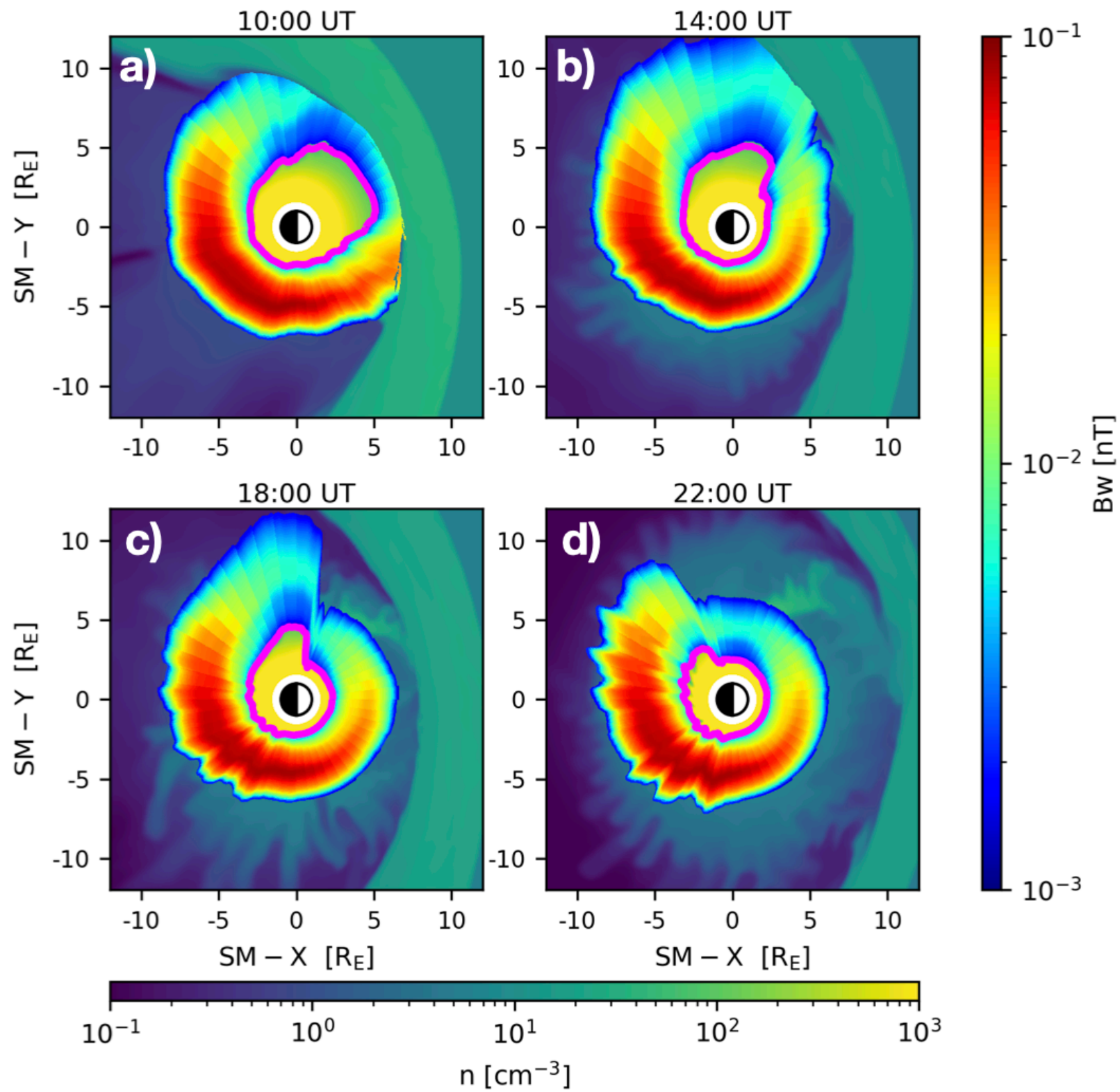


Figure 3.

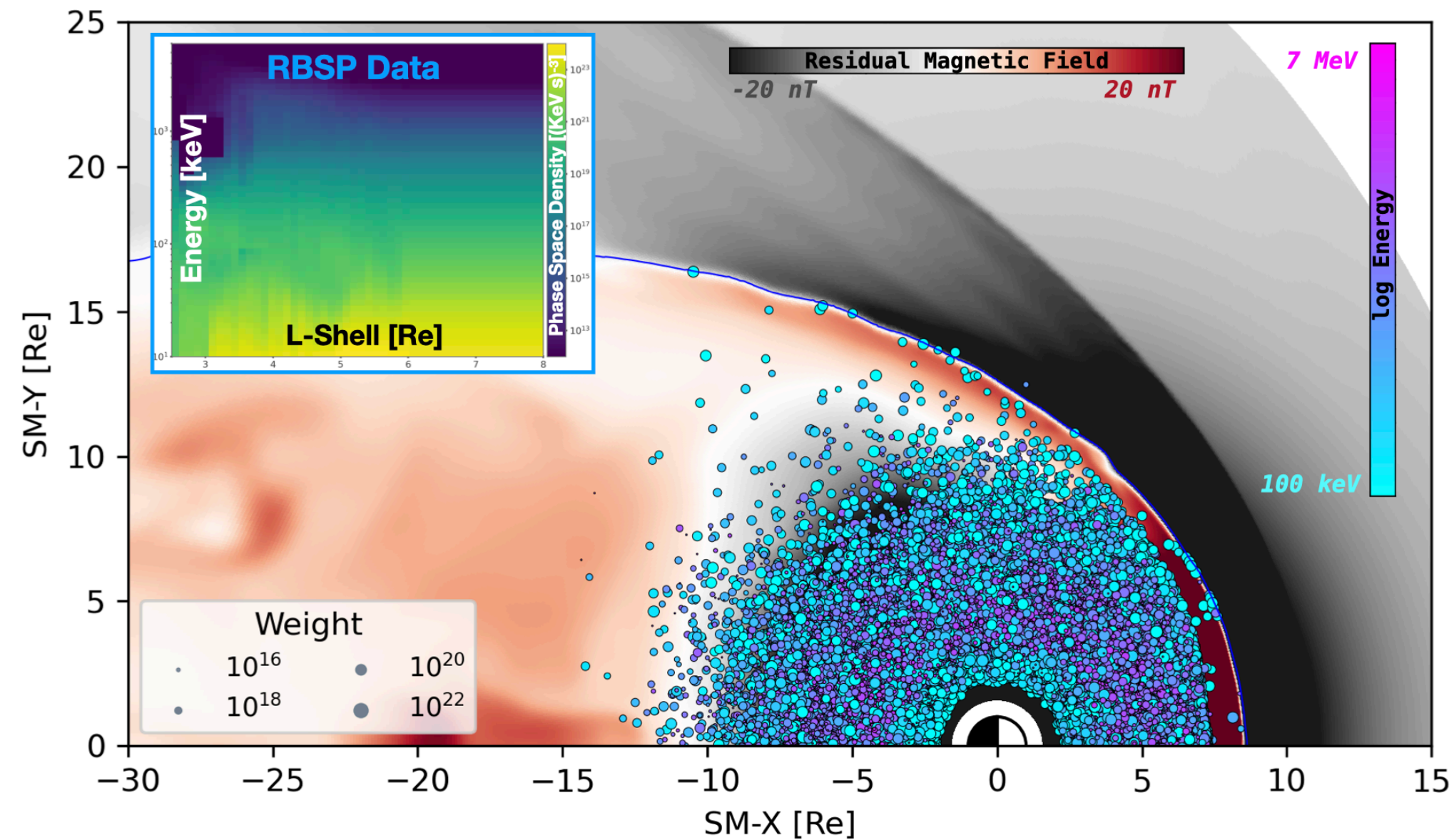


Figure 4.

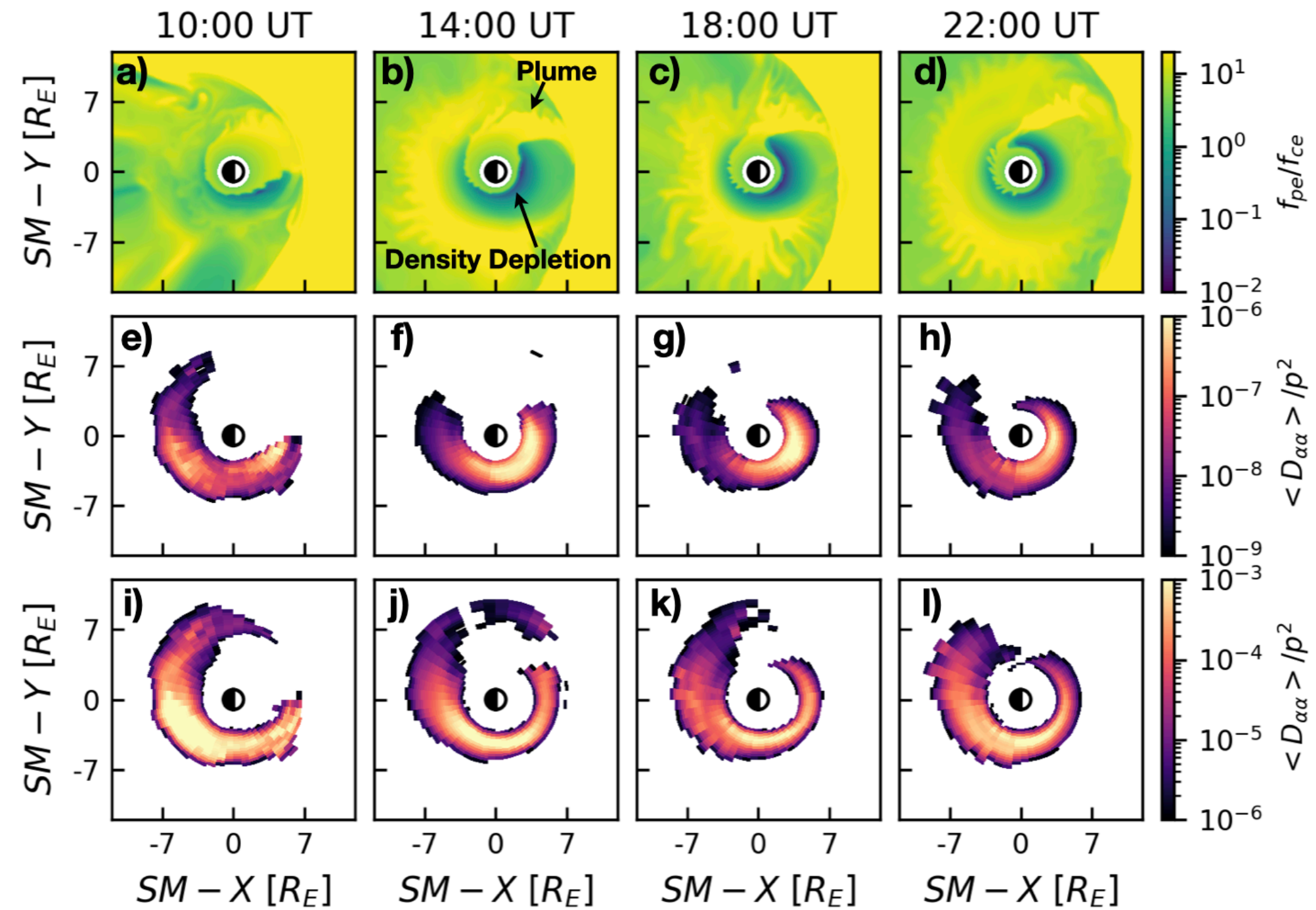


Figure 5.

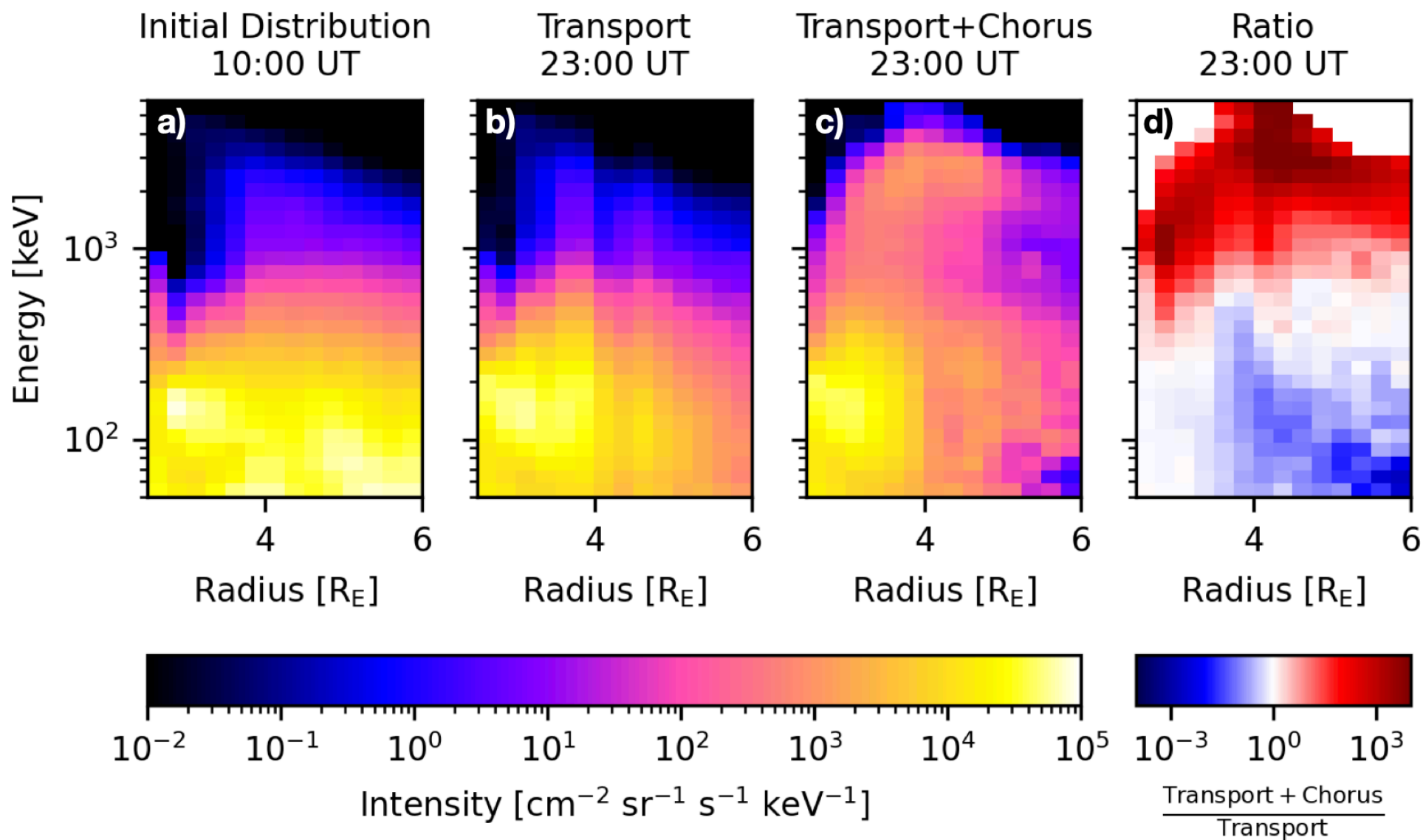


Figure 6.

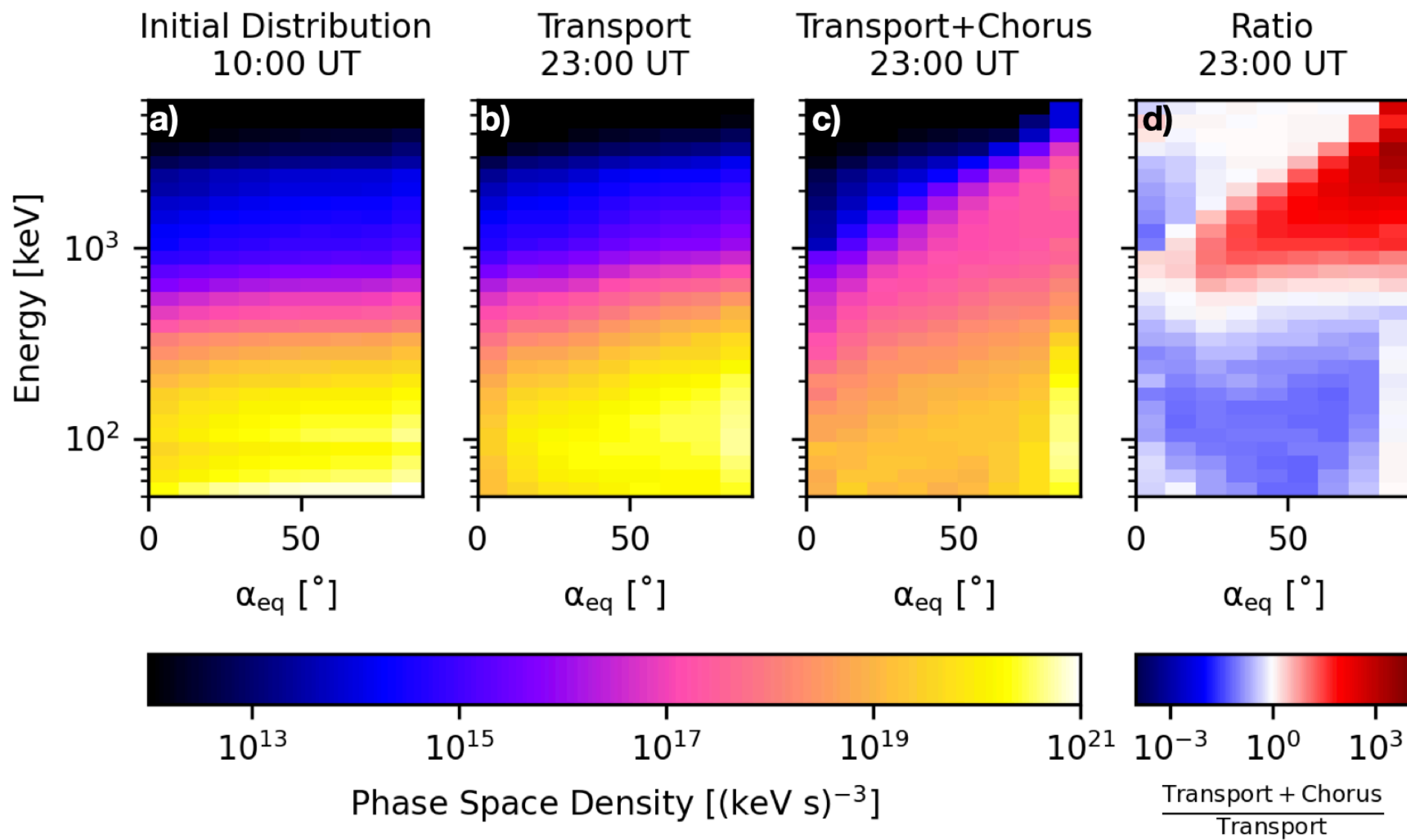


Figure 7.

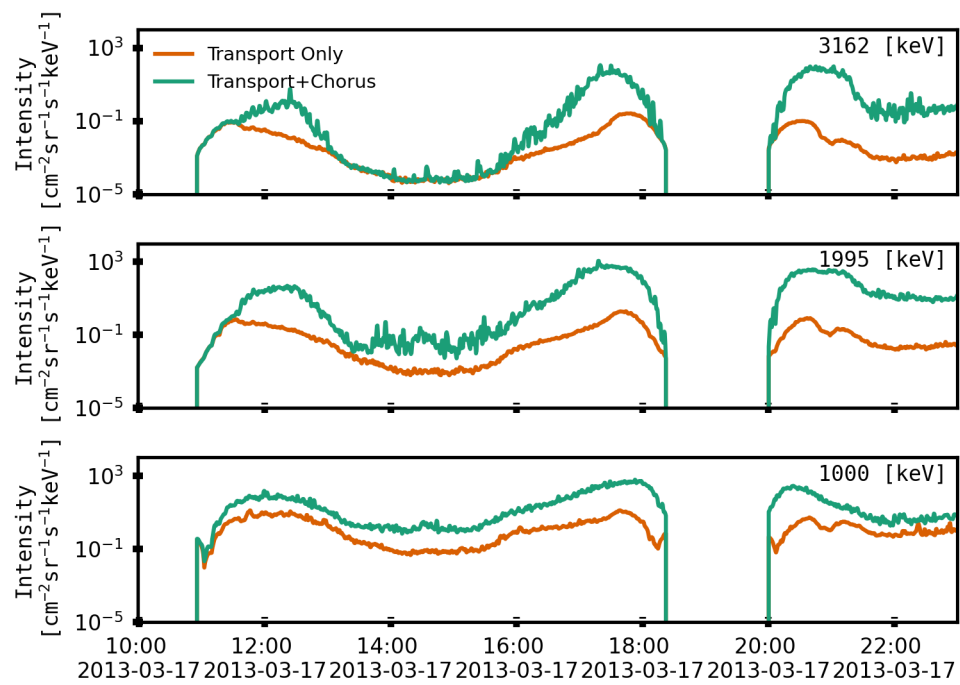


Figure 8.

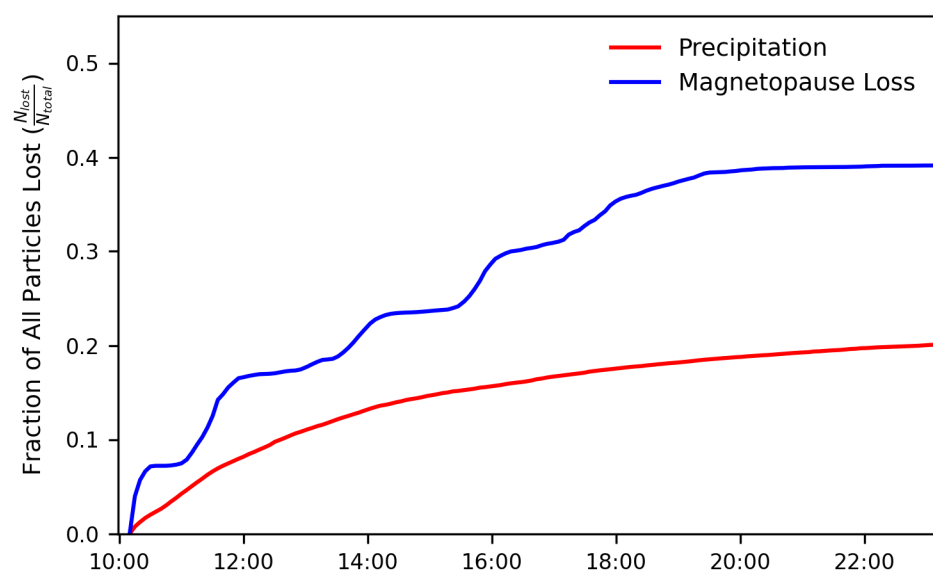


Figure 9.

